



Research
Microwave Wireless Power Transfer Technology—Review

Scavenging Microwave Wireless Power: A Unified Model, Rectenna Design Automation, and Cutting-Edge Techniques



Si-Ping Gao^a, Jun-Hui Ou^{b,c}, Xiuyin Zhang^b, Yongxin Guo^{a,*}

^a Department of Electrical and Computer Engineering, National University of Singapore, Singapore 117576, Singapore

^b School of Electronic and Information Engineering, South China University of Technology, Guangzhou 510641, China

^c School of Future Technology, South China University of Technology, Guangzhou 511442, China

ARTICLE INFO

Article history:

Received 31 October 2022

Revised 22 January 2023

Accepted 24 May 2023

Available online 8 August 2023

Keywords:

Microwave wireless power transfer
Microwave wireless energy harvesting
Unified Rectifier model
Automated rectenna design
Emerging rectenna techniques

ABSTRACT

While sufficient review articles exist on inductive short-range wireless power transfer (WPT), long-haul microwave WPT (MWPT) for solar power satellites, and ambient microwave wireless energy harvesting (MWEH) in urban areas, few studies focus on the fundamental modeling and related design automation of receiver systems. This article reviews the development of MWPT and MWEH receivers, with a focus on rectenna design automation. A novel rectifier model capable of accurately modeling the rectification process under both high and low input power is presented. The model reveals the theoretical boundary of radio frequency-to-direct current (dc) power conversion efficiency and, most importantly, enables an automated system design. The automated rectenna design flow is sequential, with the minimal engagement of iterative optimization. It covers the design automation of every module (i.e., rectifiers, matching circuits, antennae, and dc–dc converters). Scaling-up of the technique to large rectenna arrays is also possible, where the challenges in array partitioning and power combining are briefly discussed. In addition, several cutting-edge rectenna techniques for MWPT and MWEH are reviewed, including the dynamic range extension technique, the harmonics-based retro-directive technique, and the simultaneous wireless information and power transfer technique, which can be good complements to the presented automated design methodology.

© 2023 THE AUTHORS. Published by Elsevier LTD on behalf of Chinese Academy of Engineering and Higher Education Press Limited Company. This is an open access article under the CC BY-NC-ND license (<http://creativecommons.org/licenses/by-nc-nd/4.0/>).

1. Introduction

In addition to the demand for wireless communication, there is also a demand for wireless power. In fact, the concept of wireless power transfer (WPT) has been brought up since the adoption of electricity, when Heinrich Hertz proved Maxwell's theory and Tesla attempted to scale up his coil in the early 20th century [1]. Modern WPT research and development emerged from harvesting and transmitting space-based solar power (SSP) to the ground in the 1970s [2,3] and from remotely powering high-altitude platforms (including unmanned aerial vehicles, UAVs) in the 1980s [4]. Since the wireless medium used was primarily in the microwave regime, this technology was also known as microwave WPT (MWPT).

After some stagnation in the 1990s, the development of MWPT revived, with a renewed interest in powering radio frequency (RF)

identifications (RFIDs) by harvesting ambient microwave power/energy [5]. Unlike MWPT for SSP applications, microwave wireless energy harvesting (MWEH) works at short ranges and low frequencies. It is, however, limited by the available ambient microwave power capped at -50 dBm·cm⁻² in the frequency range from 500 to 3000 MHz [6]. Fig. 1 shows the ambient power density levels in Singapore. In order to better scavenge weak ambient power, a few approaches have emerged. The most straightforward way involves spatially expanding the harvesting aperture using multiple rectennas or arrays [7–9]. A similar concept applies to spectral expansion, in which the ambient power over multiple frequency channels is exploited, leading to multi-band [10] and broadband rectennas [11]. Unlike these approaches, the most disruptive way is probably boosting the rectification efficiency at low input power by leveraging low-threshold diodes (backward tunnel diodes, spin-torque diodes, etc.) [12–14]. A good review on far-field MWEH with a focus on low-power emerging applications can be found in Ref. [15].

Fig. 2 shows a typical MWPT system from the power source in a transmitter all the way to the direct current (dc) load in a receiver.

* Corresponding author.

E-mail address: yongxin.guo@nus.edu.sg (Y. Guo).

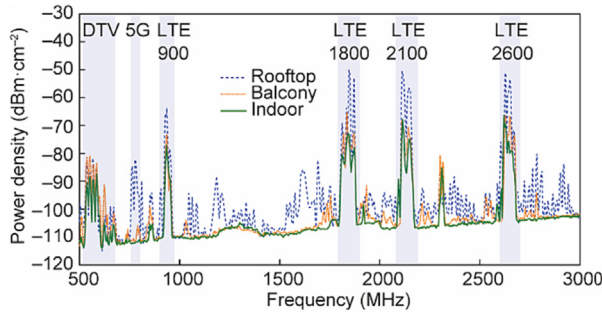


Fig. 1. Measured ambient RF power density at the National University of Singapore. Measurements were conducted on the rooftop, on the balcony, and in the Monolithic Microwave Integrated Circuit (MMIC) laboratory of block E7. DTV: digital television; LTE: long-term evolution; 5G: the fifth generation mobile communication technology.

The power source (regardless of being dedicated or ambient) comprises an oscillator, power amplifier, and transmit antenna, while the receiver includes a receive antenna, matching circuit, rectifying circuit, dc–dc converter, and dc load. For mid- and long-haul MWPTs [16,17], the dc-to-dc power conversion efficiency is the key performance indicator, while for near- and mid-range MWEH, only the RF-to-dc power conversion efficiency of the receiver is of concern. Since receivers exist for both MWPT and MWEH systems, they will be the focus of this article.

The overall RF-to-dc power conversion efficiency of a receiver after the antenna $\eta_{overall}$ can be decomposed as follows:

$$\eta_{overall} = \eta_{match} \times \eta_{rect} \times \eta_{dc-dc} \quad (1)$$

where η_{match} is the efficiency of the matching circuit between the antenna and the rectifier, η_{rect} is the RF-to-dc power conversion efficiency of the rectifier, and η_{dc-dc} is the efficiency of the dc–dc converter. To maximize $\eta_{overall}$, one needs a good match between antenna and rectifier, a high-efficiency rectifier, and a high-efficiency dc–dc converter (usually a boost converter) if the rectifier output is insufficient for the load. Other factors, including the rectenna array design [18], power combining strategy [19], and possible power scheduling and management [20], may also affect the overall performance. Nevertheless, the foundation of a receiver is always the rectifier. To achieve a good design, an accurate rectifier model is of the utmost importance.

This article reviews the development of MWPT and MWEH receivers, with a focus on rectenna design automation. A novel

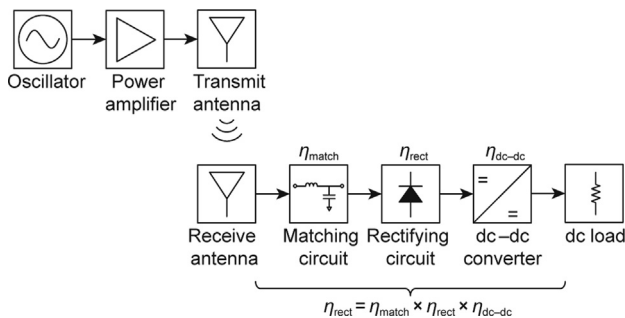


Fig. 2. A typical MWPT system consists of a transmitter and a receiver. The transmitter comprises an oscillator, power amplifier, and transmit antenna, while the receiver includes a receive antenna, matching circuit, rectifying circuit, dc–dc converter, and dc load. An MWEH system involves only the receiver. η_{match} : the efficiency of the matching circuit between the antenna and the rectifier; η_{rect} : the RF-to-dc power conversion efficiency of the rectifier; η_{dc-dc} : the efficiency of the dc–dc converter; $\eta_{overall}$: the overall RF-to-dc power conversion efficiency of the receiver after the antenna.

model, capable of accurately modeling the rectification process under both high and low input power is presented. It reveals the theoretical boundary of the rectifiers’ RF-to-dc efficiency. Based on the model, a parametric analysis is conducted, which benefits both the device tuning of rectifying diodes and the optimization of rectifier design. More importantly, an automated system design methodology is enabled. Scaling up from a single rectenna element to large rectenna arrays becomes possible, and array partitioning and power combining are thoroughly discussed. Furthermore, several cutting-edge techniques for rectenna design in MWPT and MWEH are introduced, including the dynamic range extension technique, the harmonics-based retro-directive technique, and the simultaneous wireless information and power transfer (SWIPT) technique.

2. Rectifier modeling

2.1. Development of rectifier modeling

Rectifiers are the key building blocks of rectennas. Due to their nonlinear behavior, accurate modeling of rectifiers is desirable for optimal design of rectennas in terms of efficiency, functionality, and cost. Numerical methods such as harmonic balance (HB) are widely used in rectifier design flows; however, such methods often hinder people from obtaining physical insight into the rectification phenomenon. In comparison, analytical models offer good physical insight. In specific, they are helpful in revealing the impact of circuit parameters and topologies on key performance indicators (i.e., conversion efficiency, loading condition, and input impedance). In addition, they can reveal the physical limitation of a rectifier, mainly the conversion efficiency. Most importantly, they allow the design of an MWPT/MWEH receiver system to flow automatically. Therefore, this article deals with analytical rectifier modeling.

There are two main directions for analytical rectifier modeling: ① the time-domain method and ② the harmonic expansion method. The time-domain method analyzes the input and output of a rectifier in the time domain and obtains the frequency-domain results (i.e., power conversion efficiency and input impedance) via Fourier transformation [21–23]. The time-domain analysis is intuitive, and the results are acceptable for preliminary prototyping [24–26]. However, the assumption of ideal switching characteristics for the rectifying diodes limits this method’s accuracy under low input power [12]. In comparison, the harmonic expansion method is good at modeling rectifiers under low input power, as it was initially developed for detectors [27–29]. By expanding the diode current–voltage (IV) characteristics in the square-law (low-power) region [30], the harmonic expansion method provides better accuracy at low input power, making it ideal for MWEH applications [31]. However, it is not suitable for high-power or after-breakdown (BR) situations, nor can it take multi-tone [32] and power-optimized waveform excitations [26] into consideration.

Table 1 summarizes the two modeling methods. Although they complement each other in terms of the power condition, from a design automation perspective, two models serving different scenarios are still inconvenient and the boundary between them is still unclear. A unified model capable of working under both low- and high-input powers is thus desirable.

2.2. A unified rectifier model

Based on the time-domain model, a unified rectifier model that works for both low and high powers is developed. This model preserves the advantages of time-domain models while eliminating

Table 1
Comparison of the two main directions of analytical rectifier modeling.

Model	Low input power	High input power	High input power (BR)	Efficiency calculation	Input impedance calculation	Power-optimized waveform excitation	Multi-tone excitation	Multi-stage rectifier	Features	Application
Time-domain model	No	Yes	Yes	Yes	Yes	Yes	Yes	Yes	Intuitive; flexible in incorporating various excitations	Dedicated MWPT
Harmonic expansion model	Yes	No	No	Yes	Yes	No	No	Yes	Simple implementation; accurate at low input power	Ambient MWEH

their drawbacks at low input power by considering the nonlinear diode IV characteristics. The concept was originally raised in Ref. [33] and will be discussed in detail here. Symbols that appear multiple times in this article are listed in Table 2.

Fig. 3(a) [33] shows the core equivalent circuit of a shunt-diode rectifier. It excludes the matching circuit, implying that $\eta_{\text{match}} = 100\%$. An ideal dc pass filter consisting in the rectifier load capacitance C_L is assumed, resulting in a dc path (denoted by the dashed line) for rectifier load resistance R_L . The rectifying diode (usually a Schottky diode) is represented by a series resistance R_s , a nonlinear junction resistance R_j , and a nonlinear junction capacitance C_j . The package parasitics are ignored for simplicity. R_j and C_j may be described by the IV and capacitance–voltage (CV) characteristics as follows:

$$I_j = I_s \left[\exp \left(\frac{V_j}{nV_T} \right) - 1 \right] \tag{2}$$

$$C_j = C_{j0} \left(1 - \frac{V_j}{V_{bi}} \right)^{-\gamma} \tag{3}$$

where I_s is the diode saturation current; V_j and I_j are the diode junction voltage and current, respectively; n is the diode ideality factor; $V_T = kT/q$ is the thermal voltage, where k is the Boltzmann constant, T is the junction temperature, and q is the charge of an electron; V_{bi} is the diode built-in voltage; C_{j0} is the diode zero-bias junction capacitance; and γ is the diode grading coefficient.

Fig. 3(b) depicts the typical time-domain behavior of a rectifier, where V_{in} is the input voltage of rectifier. Due to the self-bias nature of a rectifier [24], V_{in} consists of a dc term, V_0 , and an RF term, $V_1 \cos(\omega t)$:

$$V_{in} = -V_0 + V_1 \cos(\omega t) \tag{4}$$

where V_0 is output dc voltage of a rectifier, V_1 is the amplitude of RF incidence, ω is the angular operating frequency, and t is time.

V_j is often represented in a piecewise fashion according to the three states of rectification—namely, ON, OFF, and BR—in Fig. 3(b). For gigahertz applications, it is safe to ignore the phase difference between V_{in} and V_j , leading to $V_0 = V_{j0}$, $V_1 = V_{j1}$, where V_{j0} is the dc component of diode junction voltage and V_{j1} is the RF component of diode junction voltage [33]. Hence, V_j may be expressed as follows:

$$V_j = \begin{cases} V_f & \text{ON} \\ -V_0 + V_1 \cos(\omega t) & \text{OFF} \\ -V_{br} & \text{BR} \end{cases} \tag{5}$$

where V_{br} is the diode reverse BR voltage and V_f is the diode forward voltage. Based on Eq. (5), the turn-on angle θ_{on} and BR angle θ_{br} can be determined:

$$\cos\theta_{on} = \frac{V_f + V_0}{V_1} \tag{6}$$

$$\cos\theta_{br} = \frac{V_{br} - V_0}{V_1} \tag{7}$$

Since V_0 is voltage-divided from the dc average of V_j , the relationship between V_0 , θ_{on} , and θ_{br} may be obtained:

$$V_0 \frac{\pi R_s}{R_L} = (\tan\theta_{on} - \theta_{on})(V_f + V_0) - (\tan\theta_{br} - \theta_{br})(V_{br} - V_0) \tag{8}$$

Moreover, the RF input power P_{in} can be decomposed as follows:

$$P_{in} = P_{dc} + P_{loss} \tag{9}$$

where $P_{dc} = V_0^2/R_L$ is the dc output power, and P_{loss} is the dissipated power during rectification, covering the losses due to R_s , V_f , and V_{br} in their respective states.

Table 2
Nomenclature.

Symbol	Definition
A_t	Aperture size of transmit antenna
A_r	Aperture size of receive antenna
V_{in}	Input voltage of rectifier
$V_{dc-dc.in}$	Input voltage of dc–dc converter
V_0	Output (dc) voltage of rectifier
$V_{dc-dc.o}$	Output voltage of dc–dc converter
V_1	Amplitude of RF incidence
V_j	Diode junction voltage
V_{j0}	Direct current component of diode junction voltage
V_{j1}	RF component of diode junction voltage
V_T	Thermal voltage
V_f	Diode forward voltage
V_{bi}	Diode built-in voltage
V_{br}	Diode reverse breakdown voltage
C_j	Diode junction capacitance
C_{j0}	Diode zero-bias junction capacitance
C_m	Capacitance of the matching circuit
C_L	Rectifier load capacitance
C_{dc-dc}	Capacitor in a dc–dc converter
L_m	Inductance of the matching circuit
L_{dc-dc}	Inductor in a dc–dc converter
I_s	Diode saturation current
$I_{dc-dc.in}$	Input current of a dc–dc converter
$I_{dc-dc.o}$	Output current of a dc–dc converter
Z_{rect}	Input impedance of rectifier
Z_{ant}	Input impedance of antenna
$Z_{match.in}$	Input impedance of matching circuit (with rectifier)
R_{rect}	Real part of Z_{rect}
X_{rect}	Imaginary part of Z_{rect}
R_L	Rectifier load resistance
R_s	Diode series resistance
R_j	Diode junction resistance
$R_{dc-dc.in}$	Input resistance of dc–dc converter
$R_{dc-dc.o}$	Output resistance of dc–dc converter
n	Diode ideality factor
γ	Diode grading coefficient
T	Junction temperature
θ_{on}	Turn-on angle
θ_{br}	Breakdown angle
ω	Angular operating frequency
f	Operating frequency
f_s	Switching frequency of dc–dc converter
D	Duty cycle ratio of dc–dc converter
G_{ant}	Receive antenna gain
η_{dc-dc}	Efficiency of the dc–dc converter
η_{match}	Efficiency of the matching circuit between the antenna and the rectifier
η_{rect}	RF-to-dc power conversion efficiency of the rectifier
$\eta_{overall}$	Overall RF-to-dc power conversion efficiency of a receiver after the antenna
P_{in}	RF input power
P_{dc}	Direct current output power
P_{loss}	Power loss of rectification
P_{loss}^{ON,R_s}	Power loss due to R_s in ON state
P_{loss}^{ON,V_f}	Power loss due to V_f in ON state
P_{loss}^{OFF,R_s}	Power loss due to R_s in OFF state
P_{loss}^{BR,R_s}	Power loss due to R_s in BR state
$P_{loss}^{BR,V_{br}}$	Power loss due to V_{br} in BR state

$$P_{loss}^{ON,R_s} = \frac{V_0}{2R_L} (V_0 + V_f) \left(\frac{\theta_{on} \tan^2 \theta_{on}}{\tan \theta_{on} - \theta_{on}} - 3 \right) \quad (10)$$

$$P_{loss}^{ON,V_f} = \frac{V_f V_0}{R_L} \quad (11)$$

$$P_{loss}^{OFF,R_s} = \frac{R_s}{\pi} (\omega V_1 C_{j0} V_{bi}^\gamma)^2 \int_{\theta_{on}}^{\pi-\theta_{br}} \frac{\sin^2 \theta}{(V_{bi} + V_0 - V_1 \cos \theta)^{2\gamma}} d\theta \quad (12)$$

$$P_{loss}^{BR,R_s} = \frac{1}{2\pi R_s} \left[V_1 \sin \theta_{br} (4V_0 - 4V_{br} + \cos \theta_{br} V_1) + 2\theta_{br} (V_{br} - V_0)^2 + V_1^2 \theta_{br} \right] \quad (13)$$

$$P_{loss}^{BR,V_{br}} = \frac{V_{br}}{\pi R_s} (V_{br} - V_0) (\tan \theta_{br} - \theta_{br}) \quad (14)$$

where P_{loss}^{ON,R_s} is the power loss due to R_s in ON state, P_{loss}^{ON,V_f} is the power loss due to V_f in ON state, P_{loss}^{OFF,R_s} is the power loss due to R_s in OFF state, P_{loss}^{BR,R_s} is the power loss due to R_s in BR state, $P_{loss}^{BR,V_{br}}$ is the power loss due to V_{br} in BR state, and $\theta = \omega t$ is the phase angle.

Unlike conventional time-domain models [21–23], the proposed unified model considers the IV characteristics of a rectifying diode, as follows:

$$R_s I_s \left[\exp \left(\frac{V_f}{nV_T} \right) - 1 \right] = V_1 \cos(\theta_{on}/1.2) - V_0 - V_f \quad (15)$$

With Eq. (15), V_f becomes a variant, in contrast to being fixed (usually $V_f = V_{bi}$) in conventional models (Figs. 4(a) and (b)).

Once $(V_0, V_1, V_f, \theta_{on}, \theta_{br})$ are solved for any given (R_L, P_{in}) , the two key performance indicators of a rectifier—the power-conversion efficiency $\eta_{rect} = P_{dc}/P_{in}$ and the rectifier input impedance $Z_{rect} = V_1/I_1$ —can be obtained, where I_1 is the diode current at the fundamental frequency [33].

Fig. 4(c) [12] compares three rectifier models using the case of SMS7630 at 2.45 GHz, where $R_L = 1000 \Omega$. While the conventional time-domain model only provides good results at high power and the harmonic expansion method only works for lower power, it is clear that the proposed unified model combines the advantages of both models, working for both high and low powers. This is primarily due to Eq. (15) which incorporates the IV characteristics of a rectifying diode in a simple yet efficient manner.

2.3. Parametric analysis

The unified rectifier model enables parametric analysis, which benefits both the device tuning of rectifying diodes and the diode selection toward an optimal rectifier design. In this article, a study based on HSMS286x is conducted, where the operating frequency $f = 2.45$ GHz and $R_L = 5000 \Omega$. The Simulation Program with Integrated Circuit Emphasis (SPICE) model parameters of HSMS286x can be found in Table 3.

Fig. 5(a) shows the impact of n on rectifier performance. n accounts for the carrier recombination as charge carriers cross the depletion layer. It typically ranges from 1 to 2, where a larger value suggests more imperfection in the junction. This is reflected in Eq. (2), where a larger n causes lower junction current under the same input power (voltage). Hence, a larger n results in a lower η_{rect} , which can be observed from Fig. 5(a).

Fig. 5(b) shows that a higher R_s lowers η_{rect} before BR. Likewise, a higher C_{j0} lowers η_{rect} before BR (Fig. 5(c)). The higher loss due to a larger R_s and/or C_{j0} is explained by Eq. (12). In Fig. 5(d), a larger V_{br} extends the turning point of η_{rect} (i.e., the maximum efficiency point) to a higher P_{in} because a higher V_0 is supported.

An interesting observation of the V_{bi} is shown in Fig. 5(e), where V_{bi} has little influence on the rectifier performance. This is in stark contrast to the V_f sweep in Ref. [34], where a smaller V_f firmly enhances η_{rect} before BR. The result in Ref. [34] is questionable, because ① the variations in V_f and C_{j0} were ignored in Ref. [34]; and ② V_f is a dependent variable rather than a diode performance indicator. In fact, sweeping V_{bi} but keeping the other diode parameters is not realistic, because V_{bi} is physically related to R_s , C_{j0} , and V_{br} . For one diode-processing technology, a smaller (larger)

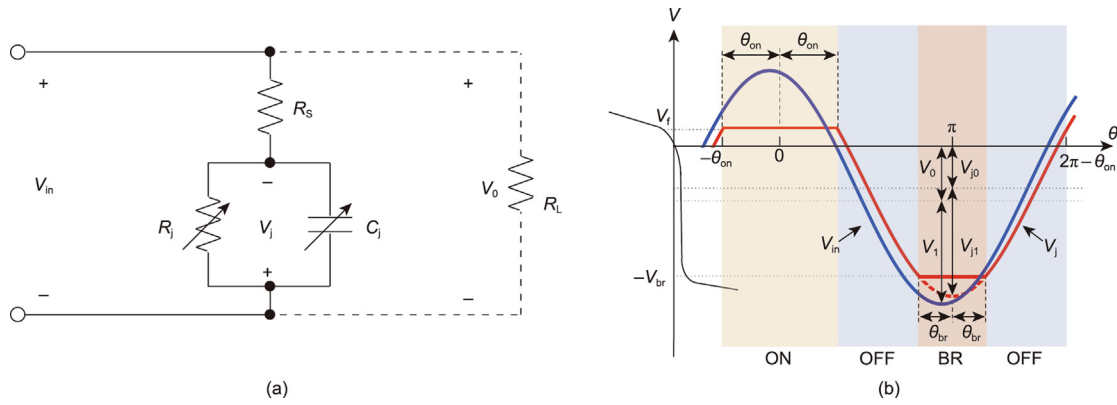


Fig. 3. Core circuit of a shunt-diode rectifier. (a) Circuit model; (b) time-domain behavior. V_{in} : input voltage of rectifier; V_0 : output (dc) voltage of a rectifier; V_j : diode junction voltage; V_{j0} : dc component of diode junction voltage; V_{j1} : RF component of diode junction voltage; R_L : rectifier load resistance; R_s : diode series resistance; R_j : diode junction resistance; C_j : diode junction capacitance; V_1 : amplitude of RF incidence; V_f : diode forward voltage; V_{br} : diode reverse BR voltage; θ_{on} : turn-on angle; θ_{br} : breakdown angle; V : instantaneous voltage; θ : phase angle. (a) Reproduced from Ref. [33] with permission.

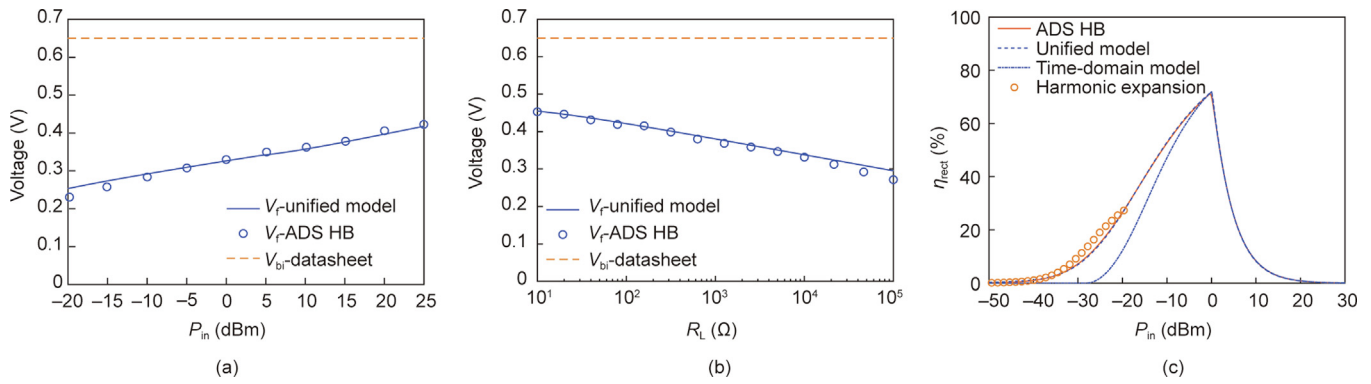


Fig. 4. V_f modeling at 2.45 GHz for HSMS286x for the cases (a) V_f versus P_{in} at $R_L = 5000 \Omega$; (b) V_f versus R_L at the maximum efficiency point. (c) Comparison between different rectifier models using a case of SMS7630 at 2.45 GHz, $R_L = 1000 \Omega$. Data for the harmonic expansion model are from Ref. [12].

V_{bi} is normally accompanied by a smaller (larger) V_{br} , smaller (larger) C_{j0} , and larger (smaller) R_s .

Therefore, considering these interrelated diode parameters, a smaller (larger) V_{bi} is expected to improve (degrade) the before-BR performance and shift the after-BR performance to a lower (higher) P_{in} . Furthermore, while only V_{br} dominates the after-BR performance, n , R_s , and C_{j0} all have an impact on the before-BR performance. Since n does not vary much among diodes, we can use the product of R_s and C_{j0} to characterize the before-BR performance of a diode. The smaller $R_s C_{j0}$ is for a diode, the higher η_{rect} is before BR, and thus the more suitable it is for low-power applications.

Figs. 5(a)–(d) show single-sided parametric studies in the absence of physical interrelation. Introducing the physical interrelation (i.e., constraint) would lead to a more comprehensive conclusion. Fig. 5(f) shows clear impact of the operating frequency on the before-BR performance. This can easily be explained by the power loss due to R_s in the OFF state in Eq. (12). Fig. 5(g) shows

that a varying load resistance R_L affects both the level and the horizontal location of the maximum efficiency point, which is of practical use. In general, a larger R_L corresponds to a smaller P_{in} . Fig. 5(h) shows another interesting phenomenon, in which a low ambient temperature has a positive impact on the rectifier performance. According to Eq. (2), a low ambient temperature causes a low V_T , leading to a higher current under the same input power (voltage). Therefore, in a cold environment, ambient microwave energy harvesting is expected to have better performance.

2.4. Contour maps

Another important application of the unified rectifier model is in the contour maps of key rectifier parameters (η_{rect} , Z_{rect}) versus independent parameters (R_L , P_{in} , f). Such contour maps can serve as lookup tables, facilitating rectenna design automation. Although

Table 3
SPICE model parameters of some proprietary diodes.

Diode	n	γ	I_s (nA)	R_s (Ω)	C_{j0} (pF)	V_{bi} (V)	V_{br} (V)	Datasheet recommendations
HSMS280x	1.08	0.5	30.0	30	1.60	0.65	75.0	High power
HSMS281x	1.08	0.5	4.8	10	1.10	0.65	25.0	High power; low flicker noise
HSMS282x	1.08	0.5	22.0	6	0.70	0.65	15.0	Medium power < 4 GHz
HSMS285x	1.06	0.5	3000.0	25	0.18	0.35	3.8	Low power < 1.5 GHz
HSMS286x	1.08	0.5	50.0	6	0.18	0.65	7.0	Medium power < 6 GHz
SMS7630	1.05	0.4	5000.0	20	0.14	0.34	2.0	Low power < 26 GHz or more

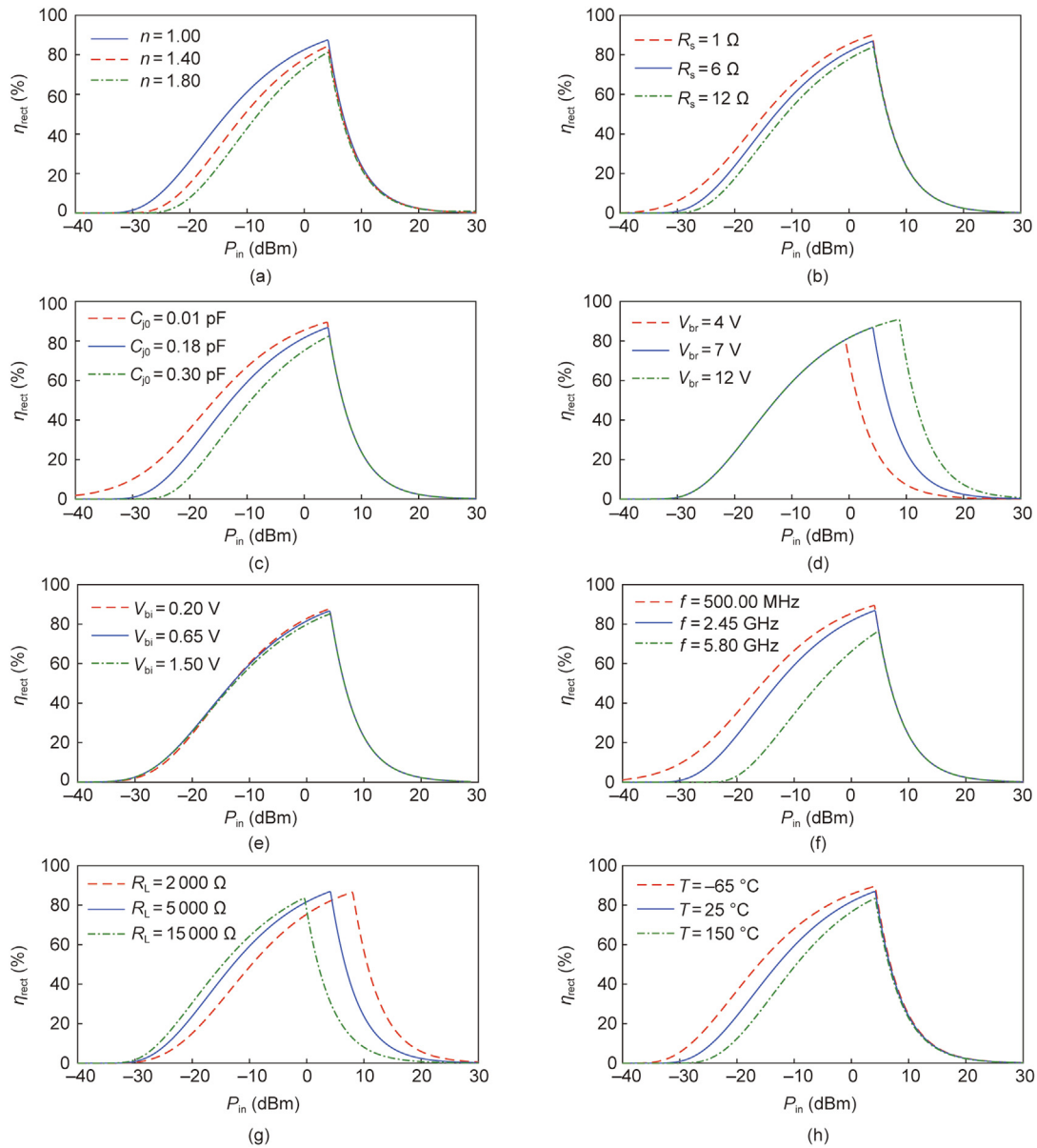


Fig. 5. Parametric analysis of diode efficiency η_{rect} versus diode and design parameters: (a) n , (b) R_s , (c) C_{j0} , (d) V_{br} , (e) V_{bi} , (f) f , (g) R_L , and (h) T . The analysis is based on HSMS286x at 2.45 GHz and $R_L = 5000 \Omega$.

ADS HB is able to model rectifiers well, specifying the power delivered to the rectifier—that is, P_{in} —is still troublesome in ADS [33]. In contrast, the unified model can take on any specific P_{in} . This allows for equidistant data generation, which is favored for contour mapping.

Figs. 6(a)–(d) [33] show contour maps of HSMS28600's key parameters over a two-dimensional (2D) plane of (R_L, P_{in}) , where the operating frequency is 2.45 GHz. The maps are built based on data generated by the unified model. A more useful form is the overlapped contour map in Fig. 6(d), where the black contour indicates the desired $\eta_{\text{rect}} (> 50\%)$, and the purple and orange lines denote the real part of Z_{rect} , R_{rect} and the imaginary part of Z_{rect} , X_{rect} , respectively. This contour map directly links the rectifier performance to the design considerations $(R_{\text{rect}}, X_{\text{rect}})$ thereby eliminating the need for iterative optimization.

While 2D contour maps facilitate single or narrow-band rectifier designs, three-dimensional (3D) contour maps over (R_L, P_{in}, f) can assist in the design of wide- and multi-band rectifiers.

Fig. 6(e) shows such a 3D map of the same diode, where the contours are now iso-surfaces of η_{rect} . The horizontal area enclosed by the η_{rect} surface shrinks as the frequency increases, indicating a more stringent design condition at higher frequencies.

2.5. Catering for various rectifier topologies

The above contour maps for a single-shunt rectifier can be easily adapted to the common rectifier topologies [35] shown in Fig. 7. Single-shunt (Fig. 7(a)) and single-series (Fig. 7(b)) topologies share the same contour maps since, theoretically, they have the same behavior [36]. The voltage doublers in Fig. 7(c) are commonly used in MWEH when the dc output voltage is insufficient for the load. Based on a voltage doubler, the Cockcroft–Walton voltage multiplier [37] and Dickson voltage multiplier [38], respectively shown in Figs. 7(d) and (e), were developed. They have similar performance, provided the requirement for capacitances is met. Differential voltage multipliers can also be constructed based on

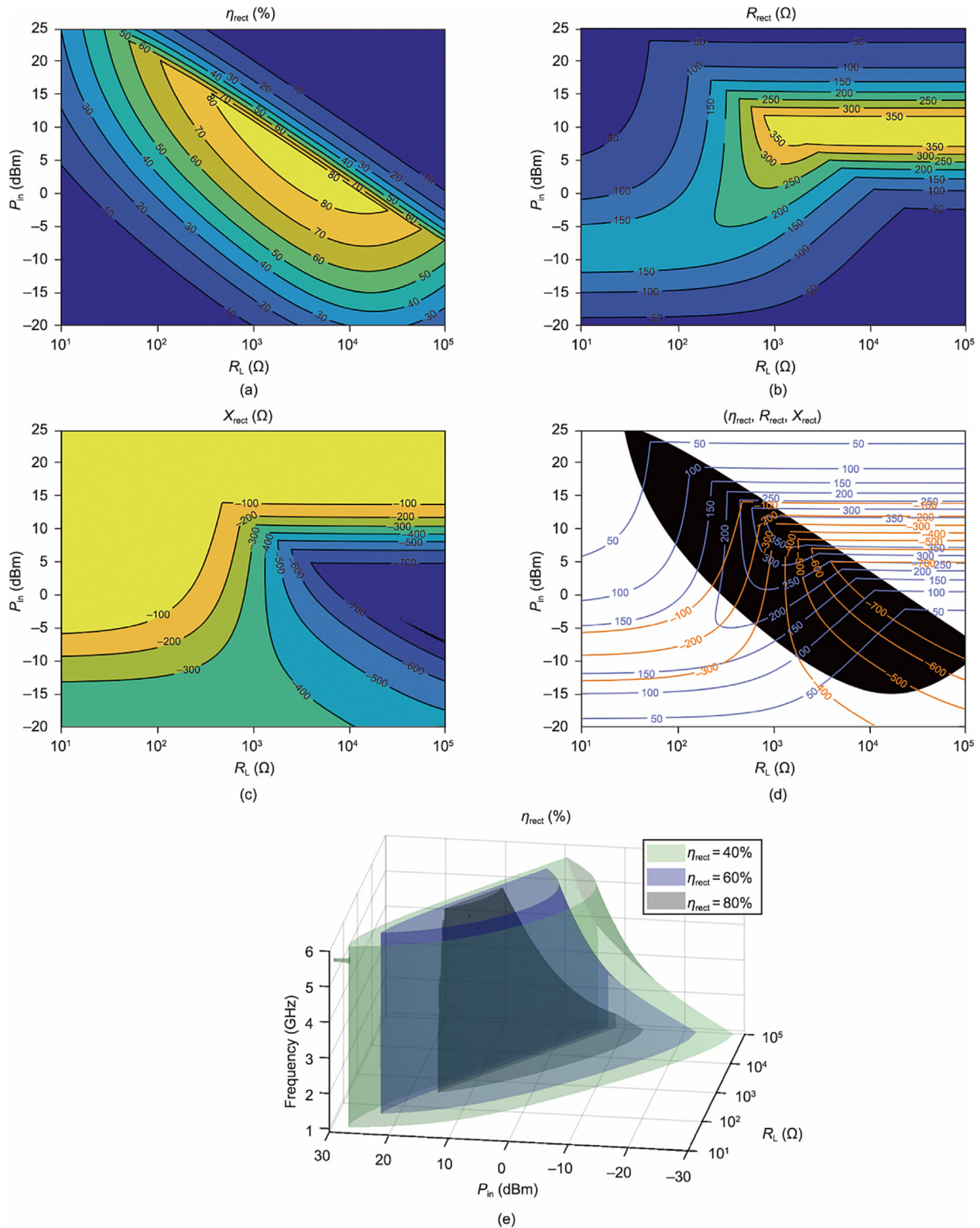


Fig. 6. Contour maps of (a) η_{rect} , (b) R_{rect} , (c) X_{rect} , and (d) $(\eta_{rect}, R_{rect}, X_{rect})$ over a two-dimensional plane (R_L, P_{in}) for HSMS2860 at 2.45 GHz, where the black contour indicates $\eta_{rect} > 50\%$, and the purple and orange lines denote R_{rect} and X_{rect} , respectively. (e) Contour map of η_{rect} over a three-dimensional space (R_L, P_{in}, f) for HSMS2860. R_{rect} : the real part of Z_{rect} ; X_{rect} : the imaginary part of Z_{rect} . (a, d) Reproduced from Ref. [33] with permission.

voltage doublers. By combining two voltage doublers, a single-stage differential voltage multiplier is formed as shown in Fig. 7(f).

Fig. 8 shows the decomposition of a voltage doubler circuit into its RF and dc loops, where the two diodes are identical. For RF

inputs, the two diodes are in parallel, because the two capacitors are short circuits. Hence, the input impedance at the RF frequency of the voltage doubler is halved compared with a single-diode rectifier $Z_{rect}^d = Z_{rect}^s/2$, where the superscripts “d” and “s” denote

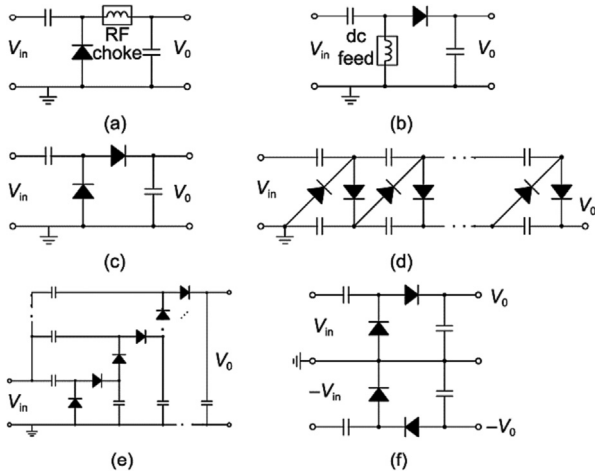


Fig. 7. Common rectifier topologies. (a) Single-shunt rectifier; (b) single-series rectifier; (c) single-stage voltage multiplier (voltage doubler); (d) N -stage Cockcroft-Walton voltage multiplier; (e) N -stage Dickson voltage multiplier; (f) single-stage differential voltage multiplier.

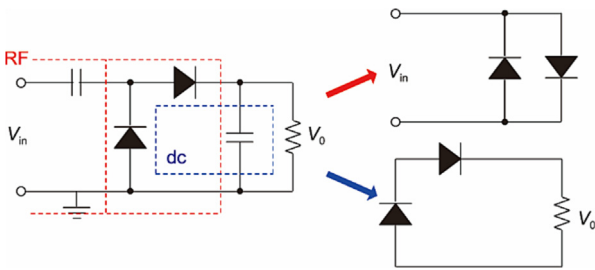


Fig. 8. Decomposition of a voltage doubler circuit into RF and dc loops.

variables of voltage doubler and single-diode rectifier, respectively; they apply throughout the article. At dc, the capacitors are open circuits; thus, the two diodes are in series, with doubled dc output voltage compared with single-diode rectifiers ($V_0^d = 2V_0^s$). For a case in which the efficiencies of a voltage doubler and a single-diode rectifier are the same ($\eta_{rect}^d = \eta_{rect}^s$), in order to sufficiently feed the two diodes in the voltage doubler, the input power must be doubled ($P_{in}^d = 2P_{in}^s$) and the load resistance must also be doubled ($R_L^d = 2R_L^s$), as the output voltage is doubled. Therefore, without any recalculation, it is possible to adapt the contour maps of single-diode rectifiers to voltage doublers via simple scaling.

In summary, the contour maps of N -stage voltage multipliers can be obtained from those of their single-diode counterparts through the operations below:

$$\begin{aligned} \eta_{rect}^N(R_L, P_{in}) &= \eta_{rect}^s\left(\frac{R_L}{2N}, \frac{P_{in}}{2N}\right) \\ Z_{rect}^N(R_L, P_{in}) &= \frac{1}{2N} \cdot Z_{rect}^s\left(\frac{R_L}{2N}, \frac{P_{in}}{2N}\right) \\ V_0^N(R_L, P_{in}) &= 2N \cdot V_0^s\left(\frac{R_L}{2N}, \frac{P_{in}}{2N}\right) \end{aligned} \quad (16)$$

where the superscript “ N ” denotes variables for N -stage voltage multipliers.

From Eq. (16), in addition to a higher dc output, voltage multipliers have a lower input impedance compared with their single-diode counterparts, which may be favorable in a matching circuit design. However, they require higher input power to achieve the same efficiency, which may be unfavorable in MWEH.

3. Rectenna design automation

3.1. Overview

In a MWPT/MWEH receiver system (Fig. 2), the rectifier is always the bottleneck, since its performance is highly sensitive to variation of the input power and load. Thus, it is reasonable to base the design automation of a rectenna or a rectenna array on that of a rectifier. Fig. 9 shows a rectifier-centric design automation flow for rectennas (or a single rectenna element in an array). It consists of four steps (in the middle row), according to the four main receiver modules shown in Fig. 2. The top row indicates the input and output of the steps, and the bottom row shows the resources and techniques required to complete these steps. The power density spectrum and the desired footprint for the system should be available beforehand, from which P_{in} can be estimated. The load information in terms of the required P_{dc} and the load variation during operation should also be known.

The flow in Fig. 9 starts with a contour-map-based automated rectifier design. The resulting Z_{rect} is used for the successive matching circuit design. Subsequently, the antenna design is carried out while considering the footprint and conjugate matching. It should be noted that the matching circuit may be ignored for the purpose of miniaturization. In the last step, a dc–dc converter is implemented to isolate the volatile dc load from the sensitive rectifier and to boost the output voltage level, if needed. The above flow can be repeated for rectenna array design automation.

3.2. Rectifier and matching circuit design

Rectifier design is an integral part of designing the whole receiver system. It can be divided into four steps: ① select the diode and the rectifier topology according to f , the available P_{in} , the required P_{dc} , and the loading information R_L ; ② determine η_{rect} and Z_{rect} ; ③ design a matching circuit between Z_{rect} and the desired input impedance of the matching circuit $Z_{match,in}$; and ④ implement the circuit and fine-tune the design. Unfortunately, due to the nonlinear nature of the circuit, rectifier design is often carried out by means of iterative optimization and tuning.

With the contour maps presented in Figs. 7 and 8, however, an automated rectifier (cum matching circuit) design can easily be achieved (Fig. 10 [33]). The use of contour maps as lookup tables helps in identifying suitable diodes and topologies to meet the requirements (P_{in} , P_{dc} , and R_L). Furthermore, from overlapped contour maps, it is possible to locate an ideal operating point (R_L, P_{in}) that fits the application. Three common applications according to regions A, B, and C are shown in Fig. 10. Once the operating point is fixed, Z_{rect} is easily read out from the overlapped contour map and used in the subsequent matching circuit design. Closed-form formulae are available for matching circuit prototypes, leading to compact designs.

The whole flow is automated and can be directly integrated into any electronic design automation (EDA) tools or form a standalone widget. Fig. 11 shows the graphic user interface (GUI) of the automated rectifier design studio (Auredest) developed based on the above technology. This tool has been used by the Internet of Things (IoT) startup WaveBoost Pte. Ltd. (Singapore), in their product development.

3.3. Antenna design

In the design flow discussed in the previous section, a matching circuit is available to bridge the gap between the impedances of the antenna and the rectifier. This makes the antenna design easy and allows for the use of off-the-shelf antennas. However, from a

miniaturization perspective, it is desirable to eliminate the matching circuit by directly conjugately matching the antenna and rectifier [39,40]. Such an elimination demands direct mapping from a desired antenna input impedance to an antenna geometry. Iterative forward modeling using full-wave solvers and inverse modeling based on neural networks [41] can do this task; however, the tuning and network training are labor intensive and time consuming. On the other hand, analytical antenna models capable of fast modeling with reasonable accuracy can easily be incorporated into the automated design flow.

Commonly used antennas in rectennas and arrays can be categorized into wire antennas [24,42], microstrip antennas [43,44], and slotted waveguide antennas [7,16]. Rectangular patch anten-

nas can be modeled by means of cavity models [45] or transmission line models [46]. The input impedance of slotted waveguide antennas can be estimated via cascading admittances [47]. In this article, we take dipole antennas as an example. For a center-fed cylindrical dipole antenna with length $2l$ and radius a (where l is the half-length of the dipole antenna), the antenna input impedance Z_{ant} can be predicted by means of the induced electromotive force (EMF) method [48].

$$Z_{ant} = \frac{j60}{\sin^2(\beta l)} \{4\cos^2(\beta l)S(\beta l) - \cos(2\beta l)S(2\beta l) - \sin(2\beta l)[2C(\beta l) - C(2\beta l)]\} \quad (17)$$

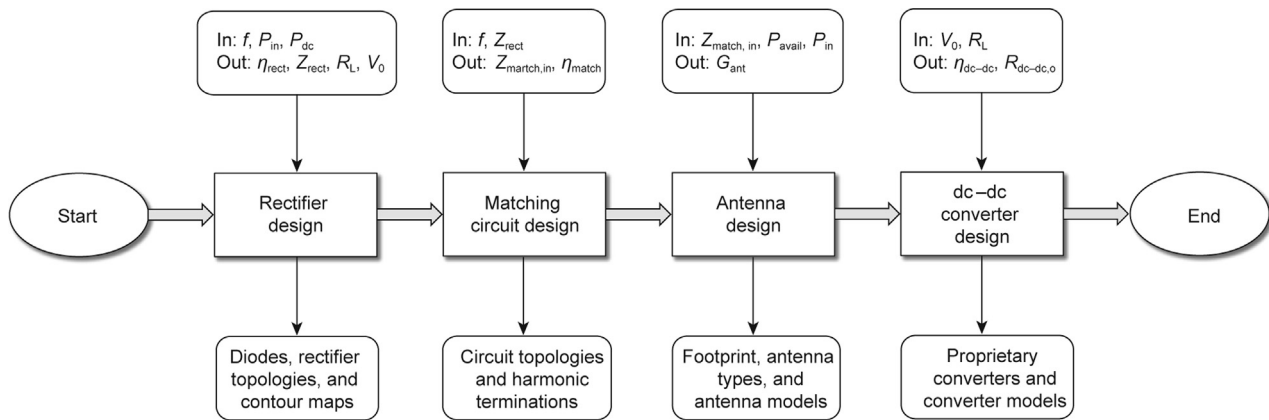


Fig. 9. The proposed rectenna design automation. The middle row shows the design flow, which consists of four main steps. The top row indicates the input and output of each step, while the bottom row shows the resources and techniques required to complete these steps. $Z_{match,in}$: the input impedance of a matching circuit (with a rectifier); P_{avail} : available power; G_{ant} : the receive antenna gain; $R_{dc-dc,o}$: the output resistance of a dc-dc converter; η_{dc-dc} : the dc-dc converter efficiency.

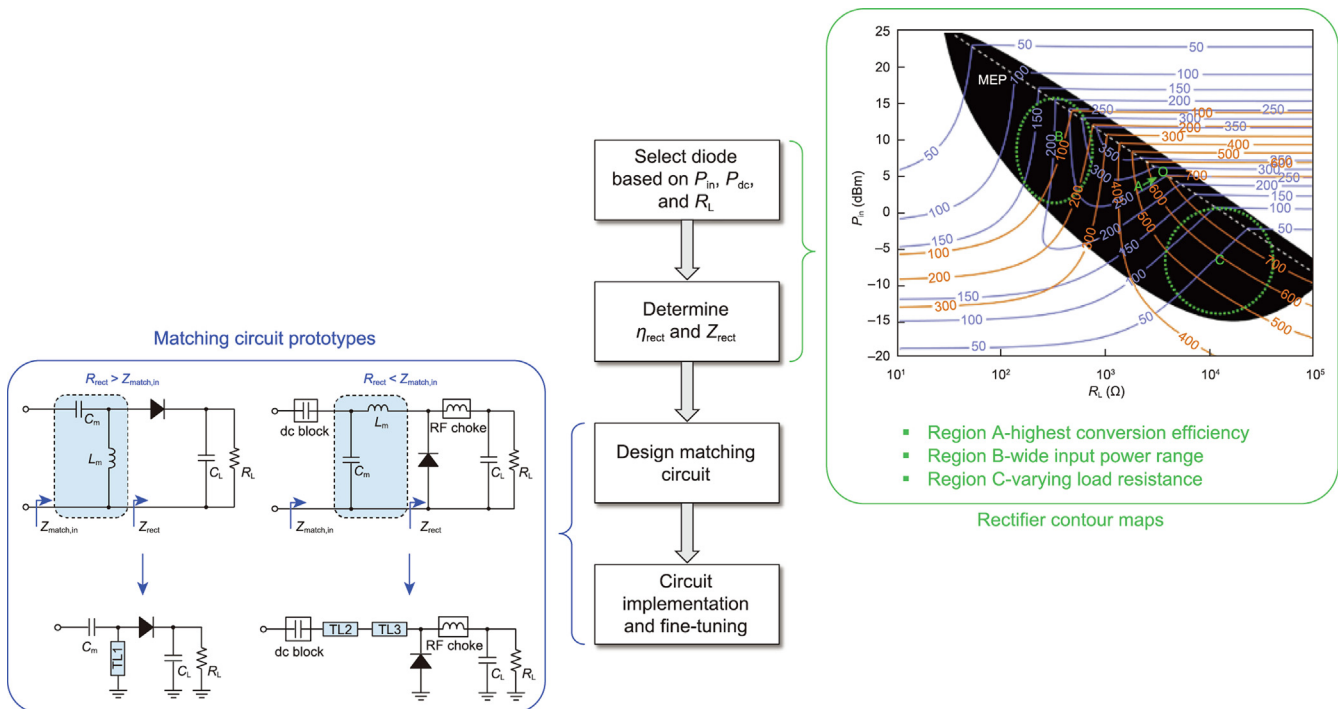


Fig. 10. Automated rectifier design flow based on contour maps and matching circuit prototypes. C_m : the capacitance of the matching circuit; L_m : the inductance of the matching circuit; TL1, TL2, TL3: the transmission lines. Reproduced from Ref. [33] with permission.

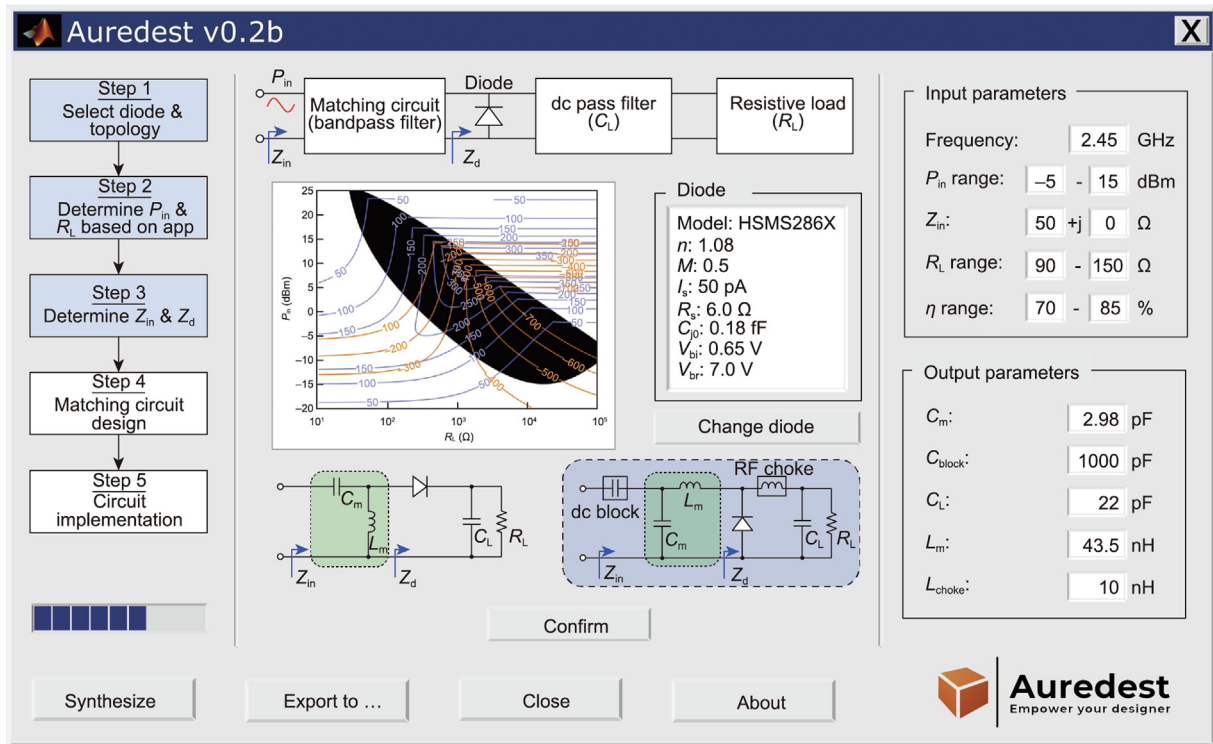


Fig. 11. GUI of an automated rectifier design tool developed based on the proposed design automation technology. GUI: graphic user interface; Z_d : diode input impedance; Z_{in} : input impedance of the rectifier; M : diode ideality factor; C_{block} : dc block capacitor; L_{choke} : RF choke inductor.

where $S(\beta l) = \frac{1}{2}Si(2\beta l) - \frac{1}{2}Cin(2\beta l) - \beta a$ and $C(\beta l) = \ln \frac{2l}{a} - \frac{1}{2}Cin(2\beta l) - \frac{1}{2}Si(2\beta l)$. β is the wave number; $Si(x)$ and $Cin(x)$ are the sine and modified cosine integrals, respectively.

Fig. 12 shows the input impedance of a center-fed cylindrical dipole antenna computed using the induced EMF method for different lengths and radii. It can be seen that the real part of Z_{ant} , R_{ant} is independent of a/λ (where λ is the operating wavelength), whereas the imaginary part of Z_{ant} , X_{ant} is more gently sloped for a larger a/λ . The typical half-wave dipoles at $2l/\lambda = 0.5$ have an impedance of $73.13 + j42.51$. With lookup tables such as Fig. 12, it is possible to identify suitable antenna physical parameters for a given target impedance (i.e., conjugate matching). The receive antenna gain G_{ant} can then be evaluated analytically or numerically

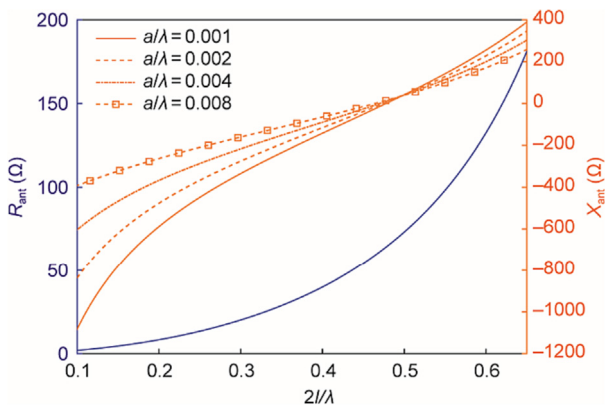


Fig. 12. Input impedance of a center-fed cylindrical dipole antenna computed via the induced EMF method for different lengths and radii.

based on the physical parameters. The analytical-model-based antenna design can be easily plugged into the previous automated rectifier design flow.

3.4. dc–dc converter design

There are two issues associated with driving a dc load in a MWPT/MWEH receiver system: ① The rectifier dc output is too low to drive any practical load; and ② the rectifier efficiency performance is sensitive to load variation. A dc–dc converter solves both problems [49].

Among switching converters, both boost converters [20] and buck-boost converters [50] are often used. Fig. 13 shows the schematic of an asynchronous boost dc–dc converter composed of an inductor L_{dc-dc} , a MOSFET switch, a diode, and a capacitor C_{dc-dc} . When the switch is closed, the inductor stores the input power as magnetic energy. The magnetic energy is released to boost the output voltage when the switch is open. In the continuous-conduction mode, the ideal input–output voltage and current relationships are as follows:

$$\begin{aligned} V_{dc-dc,o} &= \frac{V_{dc-dc,in}}{1-D} \\ I_{dc-dc,o} &= I_{dc-dc,in}(1-D) \end{aligned} \quad (18)$$

where D is the duty cycle ratio between 0 and 1, $V_{dc-dc,o}$ is the output voltage of a dc–dc converter, $V_{dc-dc,in}$ is the input voltage of a dc–dc converter, $I_{dc-dc,o}$ is the output current of a dc–dc converter, and $I_{dc-dc,in}$ is the input current of a dc–dc converter. It can be seen that $V_{dc-dc,o}$ is always greater than or equal to $V_{dc-dc,in}$. The input–output impedance (resistance) relationship is thus as follows:

$$R_{dc-dc,o} = \frac{R_{dc-dc,in}}{(1-D)^2} \quad (19)$$

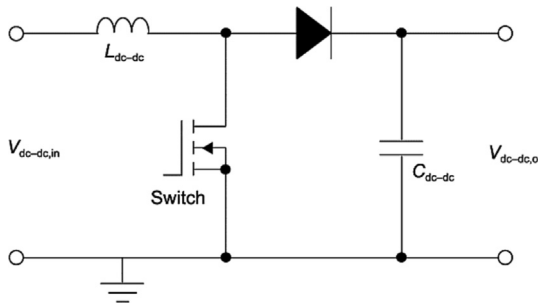


Fig. 13. Typical schematic of a boost dc-dc converter. L_{dc-dc} : the inductor of the converter; $V_{dc-dc,in}$: the input voltage of the converter; $V_{dc-dc,o}$: the output voltage of the converter; C_{dc-dc} : the capacitor of the converter.

where $R_{dc-dc,in}$ and $R_{dc-dc,o}$ are the input and output resistance of the converter, respectively.

Due to the switching operation, ripples occur in the input current and output voltage, which can be predicted by these equations:

$$\Delta I_{dc-dc,in} = \frac{V_{dc-dc,in} D}{L_{dc-dc} f_s} \quad (20)$$

$$\Delta V_{dc-dc,o} = \frac{V_{dc-dc,in} D}{C_{dc-dc} (1 - D) R_{dc-dc,o} f_s} \quad (21)$$

where f_s is the switching frequency.

Since dc-dc converter technology is mature, commercially available converter chips are often used in an MWPT/MWEH receiver system. The design then includes the determination of $R_{dc-dc,in}$, $R_{dc-dc,o}$, L_{dc-dc} , and C_{dc-dc} . Eqs. (20) and (21) help in determining L_{dc-dc} and C_{dc-dc} . $\Delta I_{dc-dc,in}$ also affects the dynamic range of R_t when a rectifier is connected in front, which should be taken into consideration in the rectifier design phase. With careful design, η_{dc-dc} can be greater than 90%.

3.5. Array design and power combining

Mid- and long-range MWPT and MWEH systems present a more complicated design challenge: namely, rectenna array synthesis,

which cannot simply be considered as a repetition of a single rectenna design. To ensure a high overall receiver efficiency, at least three key steps must be well addressed: ① the determination of the aperture size of the rectenna array, ② the array partitioning based on the available aperture power density, and ③ power combining at the RF and/or dc stages [18].

The aperture size of a rectenna array can be explained by the relationship below for close to 100% beam collection [2].

$$2.44 = \frac{\sqrt{A_t A_r}}{\lambda L} \quad (22)$$

where A_t and A_r are the transmit and receive aperture sizes, respectively; and L is the distance between the transmit and the receive antennas. It is clear that A_r is inversely proportional to A_t when the rest parameters are fixed. Transmit antenna array synthesis powered by advanced optimization methods is able to focus most of the beam within a small aperture area for the receive antenna, such that both A_t and A_r can be small [51–56].

The array partitioning depends on the available power density distribution over the receive aperture. The power density, in general, decreases from center to edge, with a few sidelobes (Fig. 14(a) [55]). Since the rectification efficiency drops sharply as the input power decreases, it is imperative to combine the weak input power at the edge of the receive aperture to form subarrays. A few subarray partitioning schemes for rectangular and circular arrays are shown in Fig. 14(b) [51], though they were originally developed for transmit antenna arrays. The rectifiers behind each subarray can be identical; thus, the number of rectifier designs is roughly equal to the number of subarray partitions. While the above design scheme is sequential (i.e., transmitter first, receiver second), a joint design of the transmit and receive systems may achieve higher overall efficiency at a lower cost.

RF power combining for subarray elements can be relatively easy to achieve; however, dc combining at the system end is a real challenge. Different rectenna subarrays have different ideal dc loads, and a direct connection can potentially degrade the overall performance. A few solutions are available, such as introducing dc power management networks (dc-dc converters) [20] and isolating dc loads with additional diodes [19]. A recent work theoretically analyzed the dc power combination of rectifiers in shunt and series topologies using an equivalent resistance method. It is found

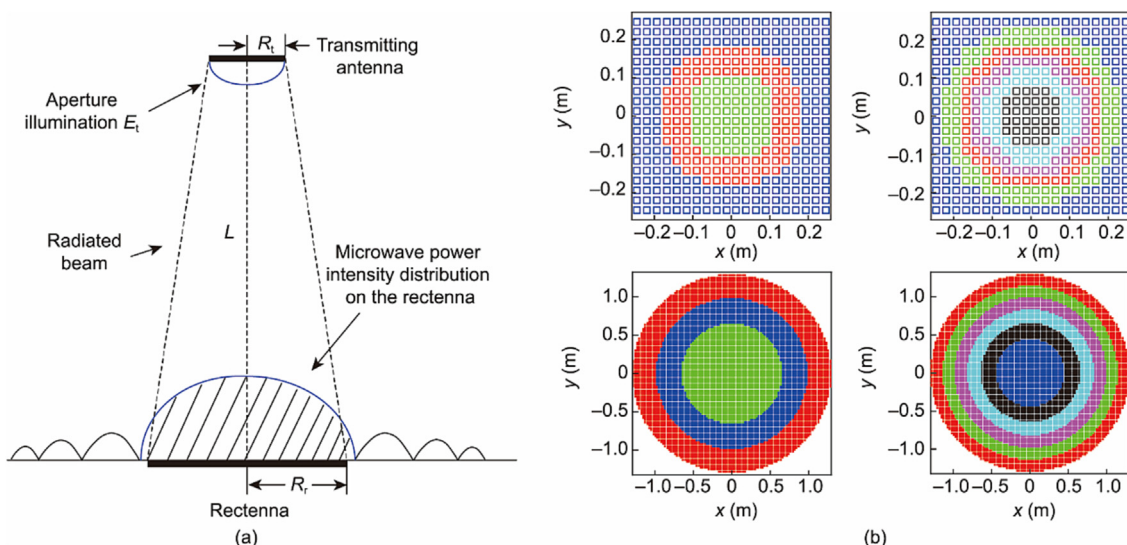


Fig. 14. (a) Typical power intensity distribution on the rectenna in a MWPT system; (b) array partitioning schemes. R_t : the radius of the transmit antenna aperture; E_t : the aperture illumination; R_r : the radius of receive antenna aperture. (a) Reproduced from Ref. [55] with permission; (b) reproduced from Ref. [51] with permission.

that the shunt topology outperforms its series counterpart under uneven power inputs [57].

4. Cutting-edge techniques

While the advances in rectenna design methodology offer new opportunities for microwave MWPT and MWEH technologies, the advent of new rectenna techniques can further strengthen and functionalize the canonical rectennas obtained from the foregoing automated design methodology. Therefore, in this section, three cutting-edge techniques—namely, the dynamic range extension, retro-directive design with harmonics, and SWIPT—will be reviewed.

4.1. Dynamic range extension technique

Due to the nonlinearity of the rectifying diode, the operating dynamic ranges of the frequency, input power, and load value are relatively narrow. To realize a high-efficiency rectifier in multi- or wide-band, some state-of-the-art works are reported here. In Refs. [10,11,58], sub-rectifiers working at different frequency bands are stacked to extend the frequency band coverage. A six-band rectifier in Ref. [2] is divided into three branches, and each branch is connected to a dual-band sub-rectifier. This allows for automatic frequency selection toward multi-band rectification.

A matching network that is effective over multi-/wide-bands is another useful technique. Such networks include π -shaped networks [59], coupled lines [60], T-shaped stubs [61], L-shaped stubs [62], cross-shaped networks [63], nonuniform transmission lines [64], multi-stage transmission lines [65], real frequency techniques [66], and frequency selective techniques [67]. By employing these elaborate networks, the frequency-dependent rectifier impedance can be matched to 50Ω over a wide bandwidth. Moreover, the bandwidth extension can be constructed by directly implementing conjugate matching between an antenna and a rectifier, as shown in Refs. [39,43,68].

For input power range extension, the multi-branch stacking technique with adaptive power distribution [69–71] can be used, where the upper and lower branches are for high and low powers, respectively. Adding a depletion-mode field-effect transistor [72–75] is another practical way to modify a conventional rectifier for a wide input power range. The modified rectifier automatically switches from low-power to high-power mode, maintaining high efficiency over a wide dynamic input power range.

Furthermore, a maximum power point tracking (MPPT) technique is proposed in Ref. [49] using a dc–dc converter. A stable and high efficiency can be maintained not only in the wide power range but also in the wide load value range. Another useful concept is power recycling [76,77]. The dynamic ranges of the input power and load value can be extended by improving the matching performance with branch-line and Lange couplers (Fig. 15 [76]).

In recent years, the resistance compression network (RCN) [78] has become popular for extending the ranges of the input power and load value, due to its simplicity and effectiveness. An RCN is able to suppress the resistance variation caused by variation in the rectifier input power and load. Based on the RCN, the impedance compression network (ICN) has been proposed [79] to directly compress the variation range of complex impedance, featuring design flexibility. To extend the frequency range at the same time, wideband RCNs and ICNs have also been developed, as illustrated in Fig. 16 [80,81]. At the same time, the input power dynamic range can be extended by reducing the input impedance variation by means of self-tuning techniques [82,83].

Along with the development of wireless communication technologies, the focus of input power dynamic range extension has shifted to the lower power bound, so that the rectenna can better harvest the ambient RF energy. That is to say, an increasing number of studies have reported enhancing the efficiency of the rectenna at a low energy density. The enhancement can be implemented at the rectifier and the antenna sides. For the rectifier part,

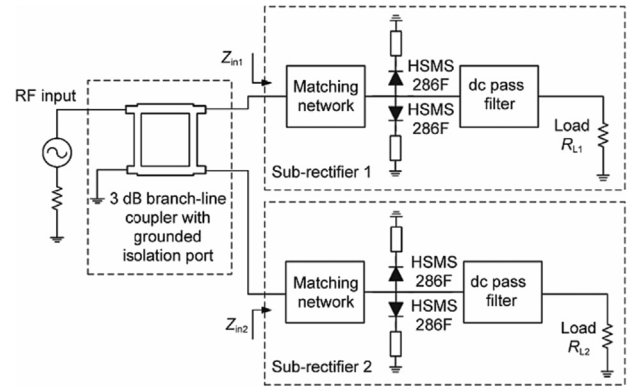


Fig. 15. A rectifier with wide ranges of input power and load value based on a branch-line coupler. Z_{in1} , Z_{in2} : the input impedances of the two rectifiers; R_{L1} , R_{L2} : the load resistances of the two rectifiers. Reproduced from Ref. [76] with permission.

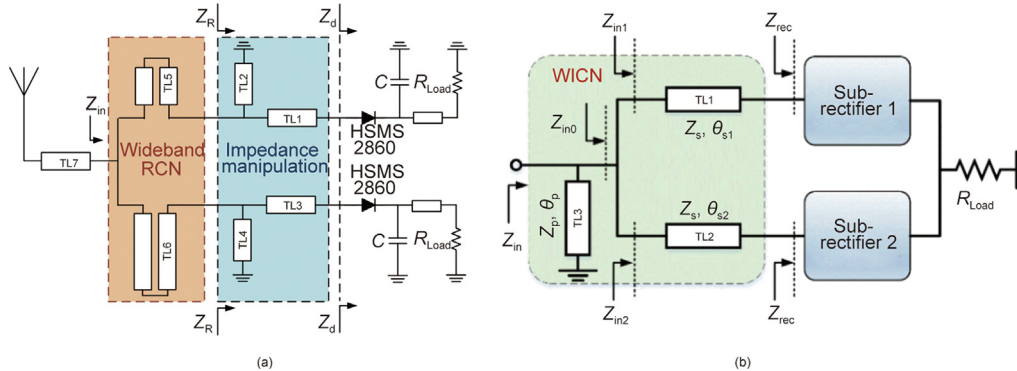


Fig. 16. Bandwidth-extended rectifiers using (a) RCN and (b) ICN. WICN: wideband impedance compression network; Z_{in} : the overall input impedance; Z_R : the rectifier input impedance; Z_d : the diode impedance; C : the load capacitance; R_{Load} : the load resistance; Z_{rec} : the rectifier input impedance; Z_s , Z_p : the characteristic impedances of transmission lines; Z_{in0} , Z_{in1} , Z_{in2} : the input impedances at different stages; θ_{s1} , θ_{s2} : the lengths of transmission lines; TL1–TL7: the transmission lines. (a) Reproduced from Ref. [80] with permission; (b) reproduced from Ref. [81] with permission.

the nonlinear behavior of the rectifying diode can be improved by means of specific circuit topologies, such as the multi-stage rectifier [84], or by improving the circuit insertion loss at low power input [85]. Low-threshold diodes specifically for low power applications have also been reported in Refs. [13,14]. For antenna elements, it is desirable to realize a larger effective receiving area at a limited size, such as the Huygens antenna [86].

Apart from the rectifier dynamic range extension, it is also desirable to achieve wide coverage of the incident wave. In wireless power transmission and wireless energy harvesting, a dual-polarized (DP) antenna is a good candidate, since it receives a linearity-polarized incident wave at any polarized tilt angle. In this case, uneven power distribution occurs at the two ports of a DP antenna under different polarized tilt angles, resulting in the efficiency fluctuation of a rectifier. To solve this problem, in Ref. [87], a 3 dB branch-line coupler is employed between the antenna and the rectifier to realize uneven-to-even power distribution.

The abovementioned techniques aim to extend only one or two aspects of the rectifier dynamic ranges, including frequency, input power, load resistance, and polarization tilt angle. In Ref. [88], by introducing a six-port coupling network, simultaneous enhancement of all the above aspects is achieved with great flexibility. This design and its outdoor demonstration are shown in Fig. 17 [88].

4.2. Harmonics-based retro-directive techniques

In radiative MWPT applications, the conversion efficiency often suffers from antenna misalignment between the transmitter and the receiver. In contrast, the unexploited harmonic power level of a rectifier is directly related to the misaligned angle, which can be exploited to realize backscattering and antenna alignment. The second harmonic is generated by a rectifier and enhanced by a power amplifier. It is then transmitted to a dual-band antenna to achieve direction-adaption [89]. However, the overall system is complicated, and such a method eliminates the possibility of recycling the second harmonic, which may take up to 25% of the total input power.

The third harmonic (weaker than its second counterpart) is thus adopted to align transmit (TX) and receive (RX) antennas [90]. A branch-line coupler is used to separate the fundamental and third harmonic powers, acting as a duplexer (Fig. 18(a) [90]). Moreover, a rat-race coupler can be exploited to realize MWPT antenna alignment using the second and third harmonics [91,92]. Circuit diagrams are depicted in Figs. 18(b) and (c) [91,92]. To ensure stable wireless links of the fundamental and second/third harmonics between TX and RX, a dual-band dual linearly-polarized (DLP) antenna is critical for allowing both high gain and necessary isolation between the vertical and horizontal polarizations. For a detailed design, interested readers are referred to Ref. [91].

The distance-adaptive MWPT based on harmonics plays an important role in micro-unmanned aerial vehicles [93], as demonstrated in Fig. 19 [90–92].

4.3. SWIPT technique based on rectifying behavior

Conventional SWIPT systems require local oscillators on the receiver side for demodulation. To eliminate the need for additional resources (i.e., hardware and power) in realizing a SWIPT system, it is desirable to exploit the rectifying behavior itself—for example, the dc output, the harmonics, and the intermodulation products—to carry information. For modulation schemes, amplitude-shift keying (ASK), phase-shift keying (PSK), frequency-shift keying (FSK), and pulse-width modulation (PWM) are often used to improve the power-conversion efficiency and transfer the information simultaneously. While high peak-to-average power ratio (PAPR) waveforms can improve the efficiency at low input power levels for far-field radiative MWPT [32,94], it is also meaningful to combine a high PAPR signal with traditional communication technology in an MWPT system.

To reduce the effect of symbol change on the rectification efficiency, traditional amplitude modulation (AM) is improved to amplitude-phase modulation (AM-PM). This technique considers the nonlinearity of diodes and improves the reliability of SWIPT systems. The combination of amplitude and phase can further

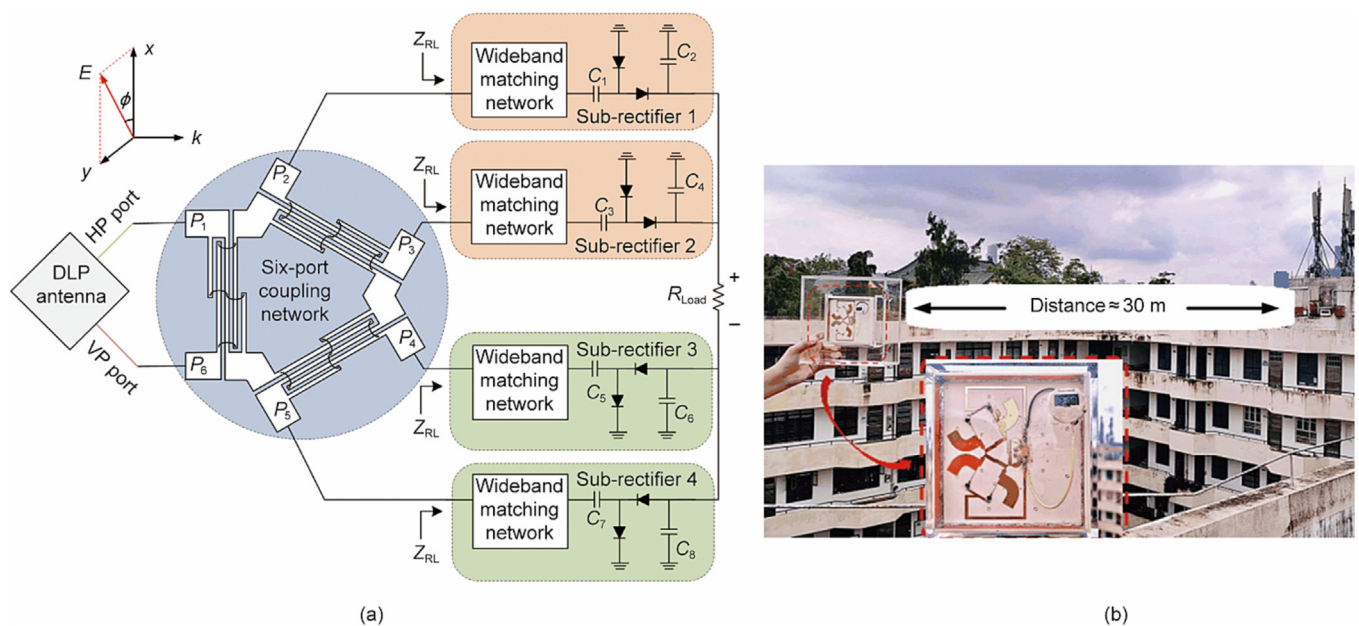


Fig. 17. (a) A multi-aspects enhanced rectifier based on a six-port coupled network and (b) its outdoor demonstration for MWEH. VP: vertical polarization; HP: horizontal polarization; DLP: dual linearly-polarized; ϕ : the polarization tilt angle; k : the wave propagation direction; E : the electric field; P_{1-6} : the ports; Z_{RL} : the input impedance of sub-rectifiers; C_{1-8} : the capacitors of sub-rectifiers. Reproduced from Ref. [88] with permission.

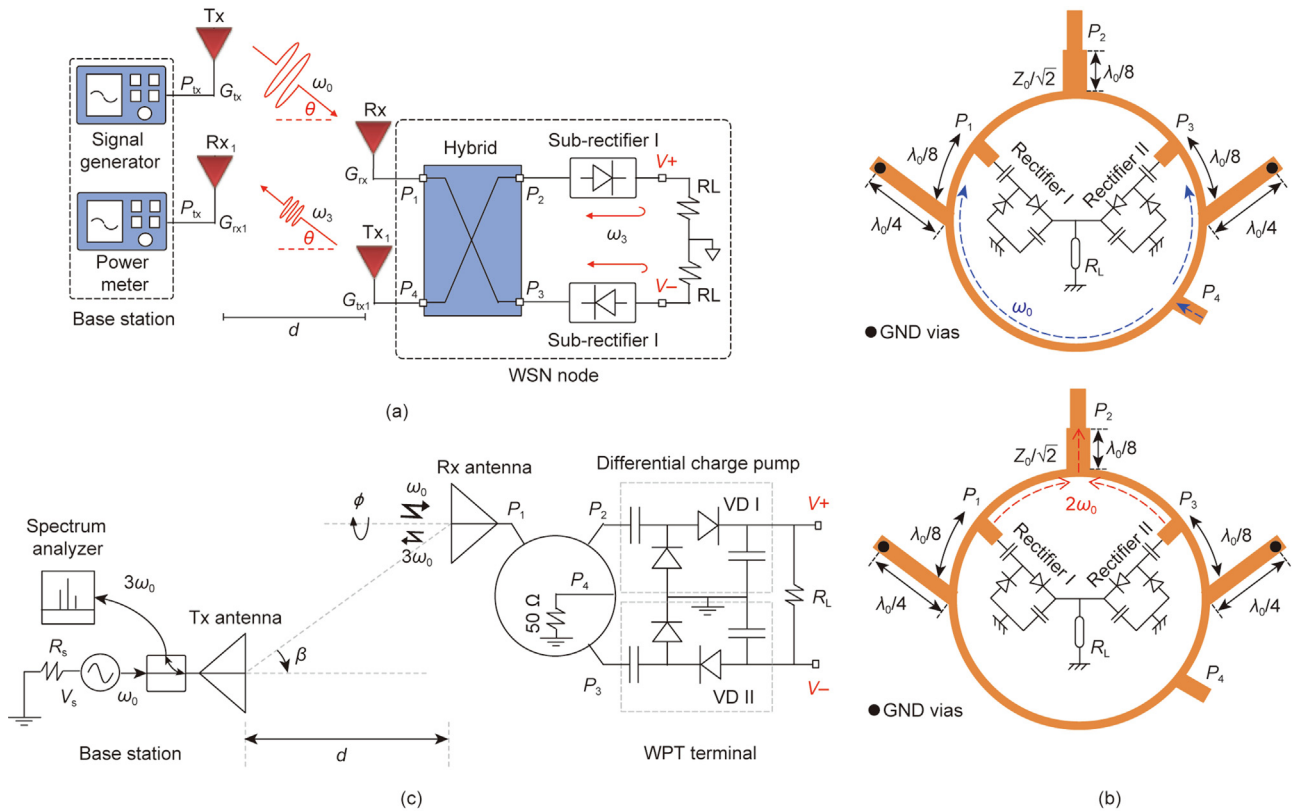


Fig. 18. MWPT antenna alignment using (a) the third harmonic with a branch-line coupler; (b) the second and (c) third harmonics with a rat-race coupler. R_L : the load resistance; WSN: the wireless sensor node; GND: the ground; VD: the voltage doubler; ω_0 : the fundamental frequency; ω_3 : the third harmonic frequency; Tx: the transmitter for ω_0 ; TX₁: the transmitter for ω_3 ; Rx: the receiver for ω_0 ; RX₁: the receiver for ω_3 ; P_{tx} : the transmit power at ω_0 ; P_{tx1} : the transmit power at ω_3 ; G_{rx} : the receive gain at ω_0 ; G_{rx1} : the receive gain at ω_3 ; G_{tx} : the transmit gain at ω_0 ; G_{tx1} : the transmit gain at ω_3 ; θ : the deviation angle; V_+ : the positive output; V_- : the negative output; Z_0 : the characteristic impedance; λ_0 : the wavelength; R_s : the source resistance; V_s : the source voltage; β : the deviation angle; d : the distance between transmitter and receiver. (a) Reproduced from Ref. [90] with permission; (b) reproduced from Ref. [91] with permission; (c) reproduced from Ref. [92] with permission.

improve the communication rate. At the receiver side, data extraction is achieved by measuring the dc voltage and the first intermodulation product. This scheme does not require a local

oscillator for demodulation, saving system resources [95]. The system test framework is shown in Fig. 20(a) [95].

In addition to modulating via amplitude and phase, frequency intervals can be used. Such a scheme adopts the FSK modulation of multi-tone signals, which improves the symbol rate to a certain extent. A system block diagram is shown in Fig. 20(b) [96], and the symbol construction is provided in Fig. 20(c) [96]. After the signal is down-converted by the rectifier hardware, a fast Fourier transform (FFT) operation is performed. Since the second-order intermodulation of the input signal changes with different frequency intervals, the symbol can be determined by measuring the second-order intermodulation of the output in FFT. The modulation of this technique does not need a local oscillator [96].

Other modulation techniques used in SWIPT are listed in Table 4 [97–100] for comparison. It can be seen that a local oscillator is not required for all the techniques. The difference between these techniques lies in the symbol construction scheme (amplitude/phase/frequency) and the corresponding demodulation technique.

Compared with traditional system architecture [101–104], the novel SWIPT technology described above, based on rectifying behavior, allows for information extraction from the rectifying product without splitting signals before a rectifier, leading to compact and reliable designs at the receive side. It is worth mentioning that, in cases requiring a minimal architecture, such as the on-body scenario, a simple dual-band dual-mode topology is a good candidate for rectenna design [105].

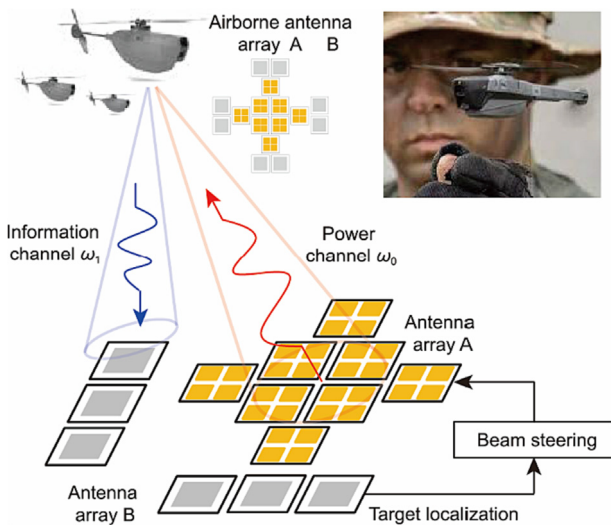


Fig. 19. Illustration of a microwave power-delivery system (backscatters ω_1 at the information channel are generated from another sub-system on UAVs).

Table 4
Comparison of SWIPT techniques using different symbol construction schemes.

Reference	Frequency	Local oscillator	Modulation	Symbol construction scheme
[97]	2.4–2.5 GHz	No	ASK-OFDM	Multitone signal
[98]	190 kHz	No	Biased-ASK	M-ASK signal
[99]	2.45 GHz	No	PSK	PSK-multi-sine
	2.45 GHz	No	QAM	QAM-multi-sine
[100]	2.45 GHz	Yes	Backscattering (uplink)	3rd order intermodulation

OFDM: the orthogonal frequency-division multiplexing; QAM: the quadrature amplitude modulation; M-ASK: multiple-order amplitude shift keying.

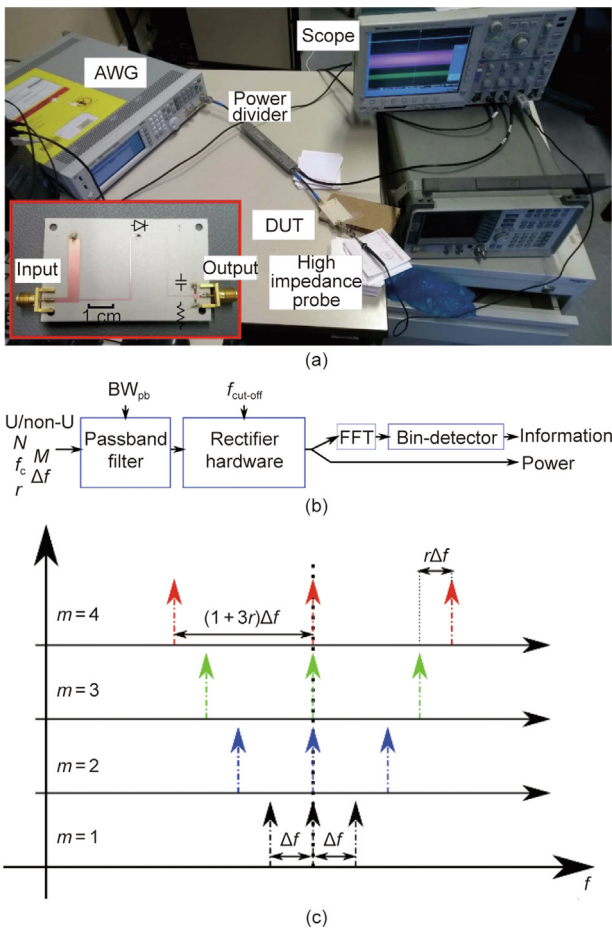


Fig. 20. (a) System test framework of an AM-PM SWIPT system. (b) System block diagram and (c) symbol construction scheme of a multitone-FSK modulation SWIPT system. AWG: the arbitrary waveform generator; DUT: the device under test; FFT: the fast Fourier transform; BW_{pb} : the passband bandwidth; $f_{cut-off}$: the rectifier's cutoff frequency; U: uniform; N: the amount of tones; M: the modulation order; f_c : the carrier frequency; r: the change in frequency spacing between symbols; m: the symbol index; f: the frequency; Δf : the frequency spacing between tones. (a) Reproduced from Ref. [95] with permission; (b, c) reproduced from Ref. [96] with permission.

5. Conclusions

This article reviewed the development of MWPT and MWEH receivers, with a focus on the design automation methodology. Starting with a brief review of rectifier models, a novel unified rectifier model that works for both low and high powers was introduced. Based on the unified rectifier model, a rectenna design automation method was presented, covering the design automation of each module (i.e., the rectifier, matching circuit, antenna, and dc-dc converter). The whole flow is sequential, with the least

possible involvement of iterative optimization and human intervention; hence, the proposed method can easily be integrated into any electronic design automation (EDA) tools. In addition, several emerging rectenna design techniques for MWPT and MWEH were reviewed, including the dynamic range extension technique, the harmonics-based retro-directive technique, and the simultaneous wireless information and power transfer technique. These can potentially strengthen the canonical designs obtained using the automated design flow.

Acknowledgments

The work is supported by the Singapore Ministry of Education Academic Research Fund Tier 1.

Compliance with ethics guidelines

Si-Ping Gao, Jun-Hui Ou, Xiuyin Zhang, and Yongxin Guo declare that they have no conflict of interest or financial conflicts to disclose.

References

- [1] Tesla N. The transmission of electrical energy without wires. *Electr World Eng* 1904;1:21–4.
- [2] Brown WC, Eves EE. Beamed microwave power transmission and its application to space. *IEEE Trans Microw Theory Tech* 1992;40(6):1239–50.
- [3] Jaffe P, McSpadden J. Energy conversion and transmission modules for space solar power. *Proc IEEE* 2013;101(6):1424–37.
- [4] East TW. A self-steering array for the sharp microwave-powered aircraft. *IEEE Trans Antennas Propag* 1992;40(12):1565–7.
- [5] Karthaus U, Fischer M. Fully integrated passive UHF RFID transponder IC with 16.7- μ W minimum RF input power. *IEEE J Solid-State Circuits* 2003;38(10):1602–8.
- [6] Piñuela M, Mitcheson PD, Lucyszyn S. Ambient RF energy harvesting in urban and semi-urban environments. *IEEE Trans Microw Theory Tech* 2013;61(7):2715–26.
- [7] Sakamoto T, Ushijima Y, Nishiyama E, Aikawa M, Toyoda I. 5.8-GHz series/parallel connected rectenna array using expandable differential rectenna units. *IEEE Trans Antennas Propag* 2013;61(9):4872–5.
- [8] Shen S, Chiu CY, Murch RD. Multiport pixel rectenna for ambient RF energy harvesting. *IEEE Trans Antennas Propag* 2018;66(2):644–56.
- [9] Vandelle E, Bui DHN, Vuong TP, Ardila G, Wu K, Hemour S. Harvesting ambient RF energy efficiently with optimal angular coverage. *IEEE Trans Antennas Propag* 2019;67(3):1862–73.
- [10] Song C, Huang Y, Carter P, Zhou J, Yuan S, Xu Q, et al. A novel six-band dual CP rectenna using improved impedance matching technique for ambient RF energy harvesting. *IEEE Trans Antennas Propag* 2016;64(7):3160–71.
- [11] Song C, Huang Y, Zhou J, Zhang J, Yuan S, Carter P. A high-efficiency broadband rectenna for ambient wireless energy harvesting. *IEEE Trans Antennas Propag* 2015;63(8):3486–95.
- [12] Hemour S, Wu K. Radio-frequency rectifier for electromagnetic energy harvesting: development path and future outlook. *Proc IEEE* 2014;102(11):1667–91.
- [13] Sayed S, Salahuddin S, Yablonovitch E. Spin-orbit torque rectifier for weak RF energy harvesting. *Appl Phys Lett* 2021;118(5):052408.
- [14] Lorenz CHP, Hemour S, Li W, Xie Y, Gauthier J, Fay P, et al. Breaking the efficiency barrier for ambient microwave power harvesting with heterojunction backward tunnel diodes. *IEEE Trans Microw Theory Tech* 2015;63(12):4544–55.
- [15] Gu X, Hemour S, Wu K. Far-field wireless power harvesting: nonlinear modeling, rectenna design, and emerging applications. *Proc IEEE* 2022;110(1):56–73.

- [16] Matsumoto H. Research on solar power satellites and microwave power transmission in Japan. *IEEE Microw Mag* 2002;3(4):36–45.
- [17] Rodenbeck CT, Jaffe PI, Strassner II BH, Hausgen PE, McSpadden JO, Kazemi H, et al. Microwave and millimeter wave power beaming. *IEEE J Microw* 2021;1(1):229–59.
- [18] Massa A, Oliveri G, Viani F, Rocca P. Array designs for long-distance wireless power transmission: state-of-the-art and innovative solutions. *Proc IEEE* 2013;101(6):1464–81.
- [19] Parks AN, Smith JR. Sifting through the airwaves: efficient and scalable multiband RF harvesting. In: *Proceedings of the 2014 IEEE International Conference on RFID; 2014 Oct 8–10; Orlando, FL, USA. New York City: IEEE; 2014. p. 74–81.*
- [20] Lee DJ, Lee SJ, Hwang IJ, Lee WS, Yu JW. Hybrid power combining rectenna array for wide incident angle coverage in RF energy transfer. *IEEE Trans Microw Theory Tech* 2017;65(9):3409–18.
- [21] Yoo TW, Chang K. Theoretical and experimental development of 10 and 35 GHz rectennas. *IEEE Trans Microw Theory Tech* 1992;40(6):1259–66.
- [22] Guo J, Zhu X. An improved analytical model for RF-DC conversion efficiency in microwave rectifiers. In: *Proceedings of the 2012 IEEE/MTT-S International Microwave Symposium Digest; 2012 Jun 17–22; Montreal, QC, Canada. New York City: IEEE; 2012. p. 1–3.*
- [23] Ou JH, Zheng SY, Andrenko AS, Li Y, Tan HZ. Novel time-domain Schottky diode modeling for microwave rectifier designs. *IEEE Trans Circuits Syst I* 2018;65(4):1234–44.
- [24] McSpadden JO, Fan L, Chang K. Design and experiments of a high-conversion-efficiency 5.8-GHz rectenna. *IEEE Trans Microw Theory Tech* 1998;46(12):2053–60.
- [25] Guo J, Zhang H, Zhu X. Theoretical analysis of RF-DC conversion efficiency for Class-F rectifiers. *IEEE Trans Microw Theory Tech* 2014;62(4):977–85.
- [26] Valenta CR, Morys MM, Durgin GD. Theoretical energy-conversion efficiency for energy-harvesting circuits under power-optimized waveform excitation. *IEEE Trans Microw Theory Tech* 2015;63(5):1758–67.
- [27] Cullen AL, An TY. Microwave characteristics of the Schottky-barrier diode power sensor. *IEE Proc H Microw Opt Antennas* 1982;129(4):191–8.
- [28] An TY, Cullen AL. Double Schottky-barrier diode power sensor. *IEE Proc H Microw Opt Antennas* 1983;130(2):160–5.
- [29] Harrison RG, Le Polozec X. Nonsquarelaw behavior of diode detectors analyzed by the Ritz-Galerkin method. *IEEE Trans Microw Theory Tech* 1994;42(5):840–6.
- [30] De Vita G, Iannaccone G. Design criteria for the RF section of UHF and microwave passive RFID transponders. *IEEE Trans Microw Theory Tech* 2005;53(9):2978–90.
- [31] Hemour S, Zhao Y, Lorenz CHP, Houssameddine D, Gui Y, Hu CM, et al. Towards low-power high-efficiency RF and microwave energy harvesting. *IEEE Trans Microw Theory Tech* 2014;62(4):965–76.
- [32] Bolos F, Blanco J, Collado A, Georgiadis A. RF energy harvesting from multitone and digitally modulated signals. *IEEE Trans Microw Theory Tech* 2016;64(6):1918–27.
- [33] Gao SP, Zhang H, Ngo T, Guo Y. Lookup-table-based automated rectifier synthesis. *IEEE Trans Microw Theory Tech* 2020;68(12):5200–10.
- [34] Valenta CR, Durgin GD. Harvesting wireless power: survey of energy-harvester conversion efficiency in far-field, wireless power transfer systems. *IEEE Microw Mag* 2014;15(4):108–20.
- [35] Lin QW, Zhang XY. Differential rectifier using resistance compression network for improving efficiency over extended input power range. *IEEE Trans Microw Theory Tech* 2016;64(9):2943–54.
- [36] Gao SP, Zhang H. Topology comparison of single-diode rectifiers: shunt diode vs. series diode. In: *Proceedings of the 12th International Workshop on the Electromagnetic Compatibility of Integrated Circuits (EMC Comp); 2019 Oct 21–23; Hangzhou, China. New York City: IEEE; 2019. p. 177–9.*
- [37] Cockcroft JD, Walton ETS. Experiments with high velocity positive ions.—(I) further developments in the method of obtaining high velocity positive ions. *Proc Math Phys Eng Sci P Roy Soc A* 1932;136(830):619–30.
- [38] Dickson JF. On-chip high-voltage generation in MNOS integrated circuits using an improved voltage multiplier technique. *IEEE J Solid-State Circuits* 1976;11(3):374–8.
- [39] Song C, Huang Y, Zhou J, Carter P, Yuan S, Xu Q, et al. Matching network elimination in broadband rectennas for high-efficiency wireless power transfer and energy harvesting. *IEEE Trans Ind Electron* 2017;64(5):3950–61.
- [40] Liu C, Lin H, He Z, Chen Z. Compact patch rectennas without impedance matching network for wireless power transmission. *IEEE Trans Microw Theory Tech* 2022;70(5):2882–90.
- [41] Swaminathan M, Torun HM, Yu H, Hejase JA, Becker WD. Demystifying machine learning for signal and power integrity problems in Packag. *IEEE Trans Compon Packag Manuf Technol* 2020;10(8):1276–95.
- [42] Sun H, Guo Y, He M, Zhong Z. Design of a high-efficiency 2.45-GHz rectenna for low-input-power energy harvesting. *IEEE Antennas Wirel Propag Lett* 2012;11:929–1922.
- [43] Song C, Huang Y, Carter P, Zhou J, Joseph SD, Li G. Novel compact and broadband frequency-selectable rectennas for a wide input-power and load impedance range. *IEEE Trans Antennas Propag* 2018;66(7):3306–16.
- [44] Hagerty JA, Helmbrecht FB, McCalpin WH, Zane R, Popovich ZB. Recycling ambient microwave energy with broad-band rectenna arrays. *IEEE Trans Microw Theory Tech* 2004;52(3):1014–24.
- [45] Gao SP, Wang B, Zhao H, Zhao WJ, Png CE. Installed radiation pattern of patch antennas: prediction based on a novel equivalent model. *IEEE Antennas Propag Mag* 2015;57(3):81–94.
- [46] Dearnley RW, Barel ARF. A broad-band transmission line model for a rectangular microstrip antenna. *IEEE Trans Antennas Propag* 1989;37(1):6–15.
- [47] Elliott RS, Kurtz LA. The design of small slot arrays. *IEEE Trans Antennas Propag* 1978;26(2):214–9.
- [48] Pistolokors AA. The radiation resistance of beam antennas. *Proc Inst Radio Eng* 1929;17(3):562–79.
- [49] Huang Y, Shinohara N, Mitani T. A constant efficiency of rectifying circuit in an extremely wide load range. *IEEE Trans Microw Theory Tech* 2014;62(4):986–93.
- [50] Fu M, Ma C, Zhu X. A cascaded boost-buck converter for high-efficiency wireless power transfer systems. *IEEE Trans Industr Inform* 2014;10(3):1972–80.
- [51] Li X, Duan B, Song L. Design of clustered planar arrays for microwave wireless power transmission. *IEEE Trans Antennas Propag* 2019;67(1):606–11.
- [52] Li X, Luk KM, Duan B. Aperture illumination designs for microwave wireless power transmission with constraints on edge tapers using Bezier curves. *IEEE Trans Antennas Propag* 2019;67(2):1380–5.
- [53] Li X, Duan B, Song L, Zhang Y, Xu W. Study of stepped amplitude distribution taper for microwave power transmission for SSPS. *IEEE Trans Antennas Propag* 2017;65(10):5396–405.
- [54] Carter PS. Circuit relations in radiating systems and applications to antenna problems. *Proc Inst Radio Eng* 1932;20(6):1004–41.
- [55] Li X, Guo YX. Multiobjective optimization design of aperture illuminations for microwave power transmission via multiobjective grey wolf optimizer. *IEEE Trans Antennas Propag* 2020;68(8):6265–76.
- [56] Li X, Luk KM, Duan B. Multiobjective optimal antenna synthesis for microwave wireless power transmission. *IEEE Trans Antennas Propag* 2019;67(4):2739–44.
- [57] Yang J, Gao SP, Zhang H, Guo Y. Analysis of series and shunt DC combination under nonuniform RF inputs using an equivalent resistance method. In: *Proceedings of the 2022 IEEE MTT-S International Wireless Symposium (IWS); 2022 Aug 12–15; Harbin, China. New York City: IEEE; 2022. p. 1–3.*
- [58] Palazzi V, Hester J, Bito J, Alimenti F, Kalialakis C, Collado A, et al. A novel ultra-lightweight multiband rectenna on paper for RF energy harvesting in the next generation LTE bands. *IEEE Trans Microw Theory Tech* 2018;66(1):366–79.
- [59] Liu J, Zhang XY, Yang CL. Analysis and design of dual-band rectifier using novel matching network. *IEEE Trans Circuits Syst II* 2018;65(4):431–5.
- [60] Lin YL, Zhang XY, Du ZX, Lin QW. High-efficiency microwave rectifier with extended operating bandwidth. *IEEE Trans Circuits Syst II* 2018;65(7):819–23.
- [61] Liu J, Huang M, Du Z. Design of compact dual-band RF rectifiers for wireless power transfer and energy harvesting. *IEEE Access* 2020;8:184901–8.
- [62] He Z, Liu C. A compact high-efficiency broadband rectifier with a wide dynamic range of input power for energy harvesting. *IEEE Microw Wirel Compon Lett* 2020;30(4):433–6.
- [63] Liu W, Huang K, Wang T, Hou J, Zhang Z. Broadband high-efficiency RF rectifier with a cross-shaped match stub of two one-eighth-wavelength transmission lines. *IEEE Microw Wirel Compon Lett* 2021;31(10):1170–3.
- [64] Kimionis J, Collado A, Tentzeris MM, Georgiadis A. Octave and decade printed UWB rectifiers based on nonuniform transmission lines for energy harvesting. *IEEE Trans Microw Theory Tech* 2017;65(11):4326–34.
- [65] Wu P, Huang SY, Zhou W, Yu W, Liu Z, Chen X, et al. Compact high-efficiency broadband rectifier with multi-stage-transmission-line matching. *IEEE Trans Circuits Syst II* 2019;66(8):1316–20.
- [66] Le G, Nguyen N, Au ND, Seo C. A broadband high-efficiency rectifier for mid-field wireless power transfer. *IEEE Microw Wirel Compon Lett* 2021;31(7):913–6.
- [67] Wu P, Huang SY, Zhou W, Liu C. One octave bandwidth rectifier with a frequency selective diode array. *IEEE Microw Wirel Compon Lett* 2018;28(11):1008–10.
- [68] Song C, Lu P, Shen S. Highly efficient omnidirectional integrated multiband wireless energy harvesters for compact sensor nodes of Internet-of-Things. *IEEE Trans Ind Electron* 2021;68(9):8128–40.
- [69] Kim J, Oh J. Compact rectifier array with wide input power and frequency ranges based on adaptive power distribution. *IEEE Microw Wirel Compon Lett* 2021;31(5):513–6.
- [70] Huang M, Lin YL, Ou JH, Zhang X, Lin QW, Che W, et al. Single- and dual-band RF rectifiers with extended input power range using automatic impedance transforming. *IEEE Trans Microw Theory Tech* 2019;67(5):1974–84.
- [71] He Z, Lan J, Liu C. Compact rectifiers with ultra-wide input power range based on nonlinear impedance characteristics of Schottky diodes. *IEEE Trans Power Electron* 2021;36(7):7407–11.
- [72] Ngo T, Huang AD, Guo YX. Analysis and design of a reconfigurable rectifier circuit for wireless power transfer. *IEEE Trans Ind Electron* 2019;66(9):7089–98.
- [73] Liu Z, Zhong Z, Guo YX. A reconfigurable diode topology for wireless power transfer with a wide power range. *IEEE Microw Wirel Compon Lett* 2016;26(10):846–8.
- [74] Liu Z, Zhong Z, Guo YX. Enhanced dual-band ambient RF energy harvesting with ultra-wide power range. *IEEE Microw Wirel Compon Lett* 2015;25(9):630–2.
- [75] Sun H, Zhong Z, Guo YX. An adaptive reconfigurable rectifier for wireless power transmission. *IEEE Microw Wirel Compon Lett* 2013;23(9):492–4.

- [76] Zhang XY, Du ZX, Xue Q. High-efficiency broadband rectifier with wide ranges of input power and output load based on branch-line coupler. *IEEE Trans Circuits Syst I* 2017;64(3):731–9.
- [77] Bo SF, Ou JH, Wang JW, Tang J, Zhang XY. Polarization-independent rectifier with wide frequency and input power ranges based on novel six-port network. *IEEE Trans Microw Theory Tech* 2021;69(11):4822–30.
- [78] Barton TW, Gordonson JM, Perreault DJ. Transmission line resistance compression networks and applications to wireless power transfer. *IEEE J Emerg Sel Top Power Electron* 2015;3(1):252–60.
- [79] Du ZX, Zhang XY. High-efficiency single- and dual-band rectifiers using a complex impedance compression network for wireless power transfer. *IEEE Trans Ind Electron* 2018;65(6):5012–22.
- [80] Du ZX, Bo SF, Cao YF, Ou JH, Zhang XY. Broadband circularly polarized rectenna with wide dynamic-power-range for efficient wireless power transfer. *IEEE Access* 2020;8:80561–71.
- [81] Bo SF, Ou JH, Zhang XY. Ultrawideband rectifier with extended dynamic-power-range based on wideband impedance compression network. *IEEE Trans Microw Theory Tech* 2022;70(8):4026–35.
- [82] Lin H, Chen X, He Z, Xiao Y, Che W, Liu C. Wide input power range X-band rectifier with dynamic capacitive self-compensation. *IEEE Microw Wirel Compon Lett* 2021;31(5):525–8.
- [83] Wu P, Huang SY, Zhou W, Ren ZH, Liu Z, Huang K, et al. High-efficient rectifier with extended input power range based on self-tuning impedance matching. *IEEE Microw Wirel Compon Lett* 2018;28(12):1116–8.
- [84] Abouzied MA, Sanchez-Sinencio E. Low-input power-level CMOS RF energy-harvesting front end. *IEEE Trans Microw Theory Tech* 2015;63(11):3794–805.
- [85] Abdelraheem A, Sinanis M, Hameedi S, Abdelfattah M, Peroulis D. A flexible virtual battery: a wearable wireless energy harvester. *IEEE Microw Mag* 2019;20(1):62–9.
- [86] Lin W, Ziolkowski RW. Electrically small, low-profile, Huygens circularly polarized antenna. *IEEE Trans Antennas Propag* 2018;66(2):636–43.
- [87] Zhang H, Gao SP, Wu W, Guo YX. Uneven-to-even power distribution for maintaining high efficiency of dual-linearly polarized rectenna. *IEEE Microw Wirel Compon Lett* 2018;28(12):1119–21.
- [88] Bo SF, Ou JH, Dong Y, Dong SW, Zhang XY. All-polarized wideband rectenna with enhanced efficiency within wide input power and load ranges. *IEEE Trans Ind Electron* 2022;69(7):7470–80.
- [89] Peng CJ, Yang SF, Huang AC, Huang TH, Chung PJ, Wu FM. Harmonic enhanced location detection technique for energy harvesting receiver with resonator coupling design. In: *Proceedings of the 2017 IEEE Wireless Power Transfer Conference (WPTC 2017)*; 2017 May 10–12; Taipei, China. New York City: IEEE; 2017.
- [90] Zhang H, Guo YX, Gao SP, Wu W. Wireless power transfer antenna alignment using third harmonic. *IEEE Microw Wirel Compon Lett* 2018;28(6):536–8.
- [91] Zhang H, Li Y, Gao SP, Guo YX. High-efficiency simultaneous wireless information and power transmission (SWIPT) by exploiting 2nd/3rd harmonics. In: *Proceedings of the 2021 IEEE International Wireless Symposium (IWS 2021)*; 2021 May 23–26; Nanjing, China. New York City: IEEE; 2021.
- [92] Zhang H, Guo YX, Gao SP, Zhong Z, Wu W. Exploiting third harmonic of differential charge pump for wireless power transfer antenna alignment. *IEEE Microw Wirel Compon Lett* 2019;29(1):71–3.
- [93] Zhang H, Guo YX. Exploiting high-isolation 2nd-harmonic backscatters for distance-adaptive microwave power delivery. In: *Proceedings of the 2021 International Applied Computational Electromagnetics Society (ACES-China) Symposium*; 2021 Jul 28–31; Chengdu, China. New York City: IEEE; 2021.
- [94] Boaventura A, Belo D, Fernandes R, Collado A, Georgiadis A, Carvalho NB. Boosting the efficiency: unconventional waveform design for efficient wireless power transfer. *IEEE Microw Mag* 2015;16(3):87–96.
- [95] Rajabi M, Pan N, Claessens S, Pollin S, Schreurs D. Modulation techniques for simultaneous wireless information and power transfer with an integrated rectifier-receiver. *IEEE Trans Microw Theory Tech* 2018;66(5):2373–85.
- [96] Claessens S, Pan N, Schreurs D, Pollin S. Multitone FSK modulation for SWIPT. *IEEE Trans Microw Theory Tech* 2019;67(5):1665–74.
- [97] Claessens S, Chang YT, Schreurs D, Pollin S. Receiving ASK-OFDM in low power SWIPT nodes without local oscillators. In: *Proceedings of the 2019 IEEE Wireless Power Transfer Conference (WPTC)*; 2019 Jun 18–21; London, UK. New York City: IEEE; 2020. p. 20–5.
- [98] Claessens S, Schreurs D, Pollin S. SWIPT with biased ASK modulation and dual-purpose hardware. In: *Proceedings of the 2017 IEEE Wireless Power Transfer Conference (WPTC 2017)*; 2017 May 10–12; Taipei, China. New York City: IEEE; 2017.
- [99] Claessens S, Rajabi M, Pan N, Pollin S, Schreurs D. Measurement-based analysis of the throughput-power level trade-off with modulated multisine signals in a SWIPT system. In: *Proceedings of the 89th ARFTG Microwave Measurement Conference (ARFTG 2017)*; 2017 Jun 9; Honolulu, HI, USA. New York City: IEEE; 2017.
- [100] Qaragoz Y, Pollin S, Schreurs D. Enhanced two-way communication for battery-free wireless sensors: SWIPT with IM3 backscattering. In: *Proceedings of the 2022 IEEE/MTT-S International Microwave Symposium*; 2022 Jun 19–24. New York City: IEEE; 2022. p. 48–51.
- [101] Zhang R, Ho CK. MIMO broadcasting for simultaneous wireless information and power transfer. *IEEE Trans Wirel Commun* 2013;12(5):1989–2001.
- [102] Abedi M, Masoumi H, Emadi MJ. Power splitting-based SWIPT systems with decoding cost. *IEEE Wirel Commun Lett* 2019;8(2):432–5.
- [103] Krikidis I, Sasaki S, Timotheou S, Ding Z. A low complexity antenna switching for joint wireless information and energy transfer in MIMO relay channels. *IEEE Trans Commun* 2014;62(5):1577–87.
- [104] Zhu GL, Du JX, Yang XX, Zhou YG, Gao S. Dual-polarized communication rectenna array for simultaneous wireless information and power transmission. *IEEE Access* 2019;7:141978–86.
- [105] Wagih M, Hilton GS, Weddell AS, Beeby S. Dual-band dual-mode textile antenna/rectenna for simultaneous wireless information and power transfer (SWIPT). *IEEE Trans Antennas Propag* 2021;69(10):6322–32.